Hist2Cell: Deciphering Fine-grained Cellular Architectures from Histology Images

Weiqin Zhao[1], Zhuo Liang[1], Xianjie Huang[2,3], Yuanhua Huang[1,2,3*], Lequan Yu[1*]

[1]Department of Statistics and Actuarial Science, The University of Hong Kong, Hong Kong SAR, China.
[2]School of Biomedical Sciences, The University of Hong Kong, Hong Kong SAR, China.
[3]Center for Translational Stem Cell Biology, Hong Kong Science and Technology Park, Hong Kong SAR, China.

*Corresponding author(s). E-mail(s): yuanhua@hku.hk; lqyu@hku.hk;
Contributing authors: wqzhao98@connect.hku.hk; tracy666@connect.hku.hk; xianjie5@connect.hku.hk;

Abstract

Histology images, with low cost, are unleashing great power of predicting cellular phenotypes in tissue, thanks to the emerging spatial transcriptomics serving as annotations. Recent efforts aimed to predict individual gene expression, suffering from low accuracy and high variability, while no methods are tailored to predict cell types - the most critical phenotype. Here, we present Hist2Cell, a Vision Graph-Transformer framework, to resolve fine-grained cell types directly from histology images and further create cellular maps of diverse tissues at a customizable resolution. Specifically, trained on human lung and breast cancer spatial transcriptome datasets, Hist2Cell accurately predicts the abundance of each cell type across space, effectively capturing their colocalization directly from histology images. Moreover, without the need for model re-training, it robustly generalizes to large-scale histology cohorts of breast cancer samples from TCGA, highlighting recurrent cell type colocalization. Therefore, Hist2Cell enables cost-efficient histology analysis for large-scale studies of spatial biology and clinical diagnostics.

Keywords: Cell Type Prediction, Spatial Transcriptomics, Computational Pathology, Graph Learning

1 Introduction

The cellular architecture of tissues, where distinct cell types are organized in space, underlies cell–cell communication, organ function, and pathology, enabling our broad and deep understanding of diverse cellular behaviours and biology. For example, cell-cell communication plays an essential role in various biological processes and functional regulations [1, 2], such as immune cooperation in a tumor microenvironment, organ development and stem cell niche maintenance, and wound healing. Emerging spatial transcriptomics (ST) technologies provide key opportunities to map resident cell types and cell signalling *in situ* in a scalable manner by probing the full transcriptome, for example Slide-seqV2 [3] and Stereo-seq [4]. Recently, several computational methods have been proposed for analyzing ST data to reveal cell variability in a tissue context. The most critical step is to characterize the cell type proportion (or abundance) in each ST spot and one of the most popular strategies is to integrate ST with the reference transcriptome signatures of cell types obtained from relevant scRNA-seq profiles. These methods started from general data interaction methods, like Seurat v3 [5] but soon embraced tailored designs for ST by modeling the read counts with negative binomial distributions (stereoscope [6], RCTD [7], and cell2location [8]), or via non-negative matrix

factorization (spotlight [9]), or as a mapping from individual cells (e.g., Tangram [10] and TransImp [11]). Of note, among these methods, cell2location uniquely provides an estimate of the absolute cell abundance on top of its proportion; also, its Bayesian treatment enables a higher sensitivity and resolution by accounting for uncertainty in technical sources of variation and borrowing statistical strength across locations; therefore, it was employed for cell type abundance estimation here.

Considering that current sequencing-based ST technologies generally suffer from low spatial resolution and low RNA capture efficiency (and sequencing depth), recent efforts have also been made to take advantage of the paired histology image to enhance ST analysis. Prominent examples include XFuse, which uses a variational autoencoder to generate super-resolution transcriptome by sharing a latent variable between ST and its image [12], while TESLA [13] and iSTAR [14] further accelerate the computational efficiency of this task via graph-based smoothing. Additionally, SpatialScope [15] utilizes histology to segment cell nuclei and achieves a single-cell level transcriptome resolution through a deep generative model (i.e., diffusion model).

However, a key limitation of these existing approaches is the requirement of estimating from spatial transcriptome data, which hinders large-scale studies due to the expensive costs. Relatively, histology images are much cheaper and easier to acquire and are routinely used in clinics [16]. Previous studies have shown that histological images are highly correlated with gene expression and cell type identification, and have been used to predict bulk gene expression profiles [17], coarse-grained cell type abundance [18], and genomic abberations [19]. Furthermore, powered by the ST technologies that provide a large amount of high-quality training data, multiple attempts were made to directly predict the expression of a set of critical genes or the full transcriptome from a cell-size path of image [17, 20–23]. However, these methods that aim to predict the expression of individual genes were generally reported with limited accuracy, probably due to the lack of predictive information for most genes. Instead, how to identify fine-grained cell-type spatial variations and infer cell-cell communication directly from histology images is underexplored and remains an open problem. Moreover, existing methods are also incapable of creating more detailed cellular wiring diagrams for higher-resolution analysis when estimating from spatial transcriptome data, as they ignore the information provided by the histology images.

In this paper, we present Hist2Cell, a Graph-Transformer framework to resolve fine-grained cell types directly from haematoxylin-and-eosin-stained histology images and create cellular maps of diverse tissues. Hist2Cell was trained on spatial transcriptome data sets for human lung [24] and human breast cancer [25] with spot-level cell abundance estimations from cell2location [8] algorithm. For held-out test patients, Hist2Cell can predict the spatial variations in the localization of fine-grained cell types - at a resolution of around 100µm, serving as important references for biological research. Specifically, it can predict substantial variation in cell localization within regions labeled as tumors or different tissue structures by clinicians, demonstrating that Hist2Cell captures significant tissue heterogeneity. By feeding the predictions to an existing toolbox like SpatialDM [26], Hist2Cell can also reveal accurate cell-type colocalizations, figuring out the prioritization of communicating cells as well as the identification of interaction spots in the spatial context. Hist2Cell is more accurate than deep learning methods that predict cell abundance solely from a single histology image spot or a limited neighboring context, as it leverages both local and global correlations of histology image spots with the proposed Graph-Transformer architecture while maintaining data diversity with a random subgraph sampling strategy.

As independent external tests, Hist2Cell accurately predicts the spatial distribution of cell types and their localization in breast cancer data from an external source [17] without any framework modification or fine-tuning. This suggests that Hist2Cell can robustly generalize to new samples despite potential batch effects or technique differences of imaging. As a result, Hist2Cell could perform large-scale cellular analysis on public histology cohorts, providing significant consensus findings for clinical applications. More importantly, Hist2Cell can provide the above analysis under a higher spatial resolution than the original spatial transcriptome technique by imputing from low-resolution cellular maps or directly predicting from histology images. In general, Hist2Cell paves the way for reliable and high-resolution investigations of cellular organization and communication in diverse tissues in a cost-efficient manner, with potential applications in diagnostics and personalized medicine.

2 Results

A schematic figure illustrating the workflow of Hist2Cell is presented in Figure 1, along with a summary of example downstream tasks depicted. Initially, Hist2Cell crops the entire slide image into a multitude of spot patches, with spot size $150 \times 150 \mu m^2$ according to the ST platforms. Treating spots as nodes and their spatial

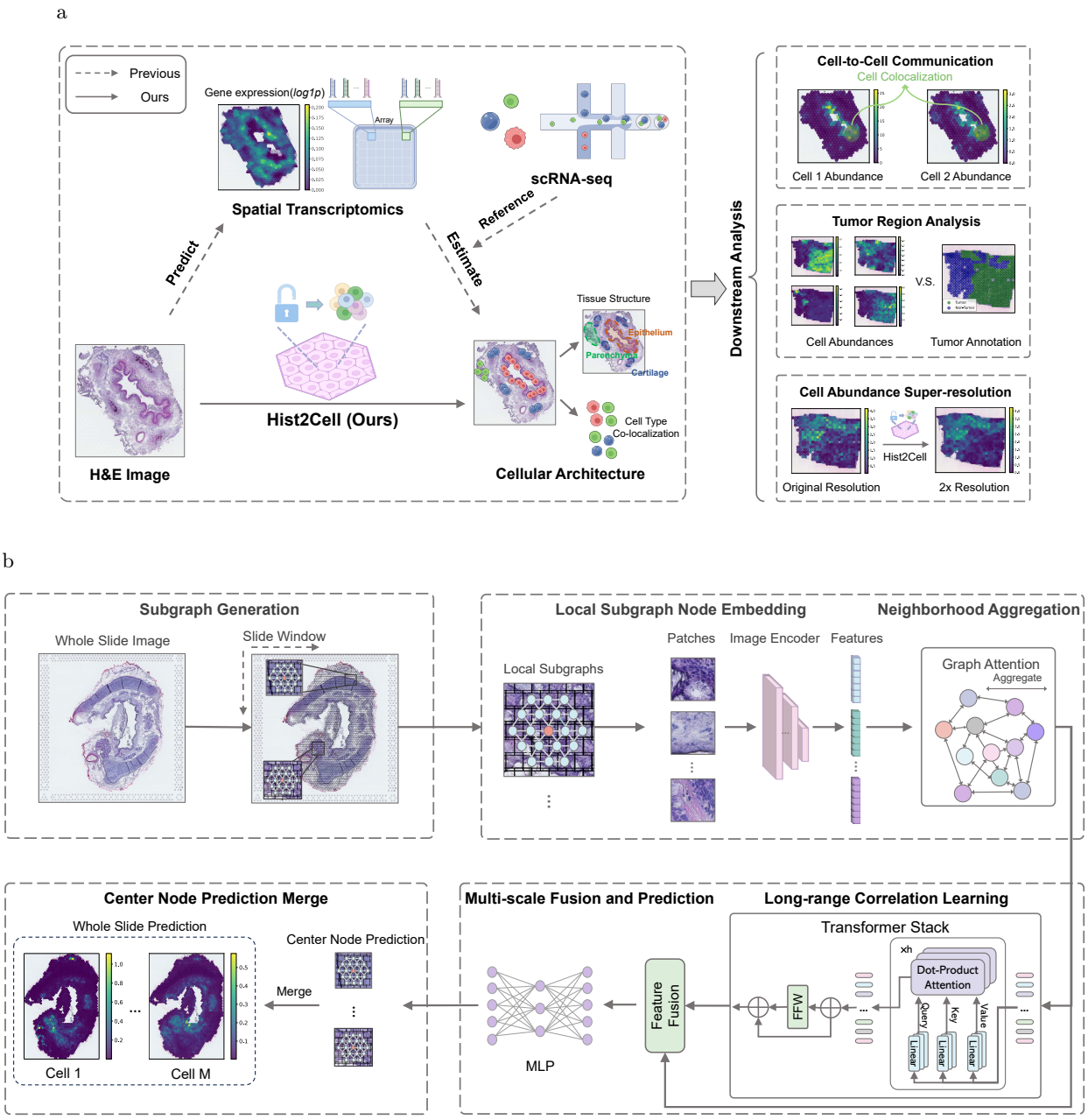

Fig. 1: **Overview of Hist2Cell. a,** Left: An illustration demonstrating how Hist2Cell directly predicts spatial cell abundance from histology images, in contrast to how previous works estimate spatial cell abundance from spatial transcriptomics data using scRNA-seq data as a reference. Right: The three major downstream tasks based on spatial cell abundance predictions by Hist2Cell - encompassing cell-cell colocalization analysis, tumor region analysis, and spatial cell abundance super-resolution. **b,** Hist2Cell initially formulates the whole slide image into a spatial graph, followed by sampling local subgraphs as input for the model. It employs a feature encoder, Graph Attention layers, and transformer layers to learn and extract the morphological features of the tissue, as well as to discern both local and long correlations among histology spots. Multi-scale features from these components are fused for fine-grained spot cell abundance prediction. The prediction for the central node of the sampled subgraphs is used as the final output during the inference phase.

neighboring relationships as edges, the whole slide image is formulated into a graph. Subsequently, multiple

subgraphs are randomly sampled from the whole slide image to serve as training inputs for Hist2Cell. Each subgraph consists of a central node and its k-hop spatial neighborhood. Following this, an image encoder extracts node embeddings from the images constituting each subgraph. Hist2Cell then employs a Graph-Transformer architecture to learn and integrate both short-range local and long-range global relationships among a batch of subgraphs from the same whole slide image, thereby enhancing the prediction of cell abundance for each node. The image encoder and the Graph-Transformer architecture are concurrently trained in an end-to-end fashion, minimizing the distance between the cell abundance predictions and ground truth labels estimated from the spatial transcriptome data. In the inference phase, Hist2Cell uses the predictions of the center nodes as the conclusive prediction and implements a sliding-window strategy to ascertain the cell abundance prediction for all spots. To assess the effectiveness of Hist2Cell, we study healthy human lung and human breast cancer tissues and a large-scale TCGA histology image dataset.

2.1 Hist2Cell Maps Cellular Architectures and Detects Key Colocalized Cell Types in Human Lung Tissues

To validate Hist2Cell, we initially applied the framework to data from 5 proximal-to-distal locations in healthy human lungs from 4 donors [24]. This dataset provides 11 haematoxylin-and-eosin-stained histology slides, resulting in a total of 20,770 spots with 80 fine-grained cell-type abundances estimated by cell2location algorithm according to the authors. More details about the 80 cell types can be found in the Supplementary Fig. 1. All performance comparisons, visualizations, and analyses are reported using leave-one-donor-out cross-validation, where we iteratively trained Hist2Cell on three of the donors and made predictions on the remaining held-out donor.

Cell Type Identification. As depicted in Fig.2.a, the cell type identification performance of Hist2Cellwas compared with methods designed for predicting local gene expression from histology images (STNet[17]), as well as variants of Hist2Cell focusing solely on short-range or long-range relations among spots. Hist2Cell demonstrated more accurate predictions of cell type abundances across locations compared to other methods, as evidenced by the overall Pearson correlations of all folds. Specifically, the analysis revealed that for 79 out of 80 cell types, the predicted cell abundance from Hist2Cell positively correlated with the provided cell abundance labels across all patients, with an average Pearson's correlation of 0.31 among all 80 cell types and patients, demonstrating a performance with 24% increase from that of STNet. These results suggest that Hist2Cell can decode fine-grained cellular architectures directly from histology images by modelling the tissue morphology feature, local context interactions, and long-range correlations with the slide. Particularly, Hist2Cell showed significantly high positive correlations with several key cell types, including CD4+ effector memory T cells (CD4 EM Effector), CD8 EM, ciliated cells, and gamma-delta T (gdT) cells (Pearson's R>0.61 and Jason-Shannon Divergences (JSD)<0.32; Fig. 2.d). Note that these highly predictable cell types have critical functions in the human airway system, for example, CD8 EM cells are essential in directly eliminating infected or malignant cells in situ [27], and ciliated cells play a pivotal role in airway homeostasis by trapping and expelling microorganisms, mucus and other debris [28]. Systematically, we also found Hist2Cell excelled in predicting the abundance for cell types exhibiting a higher spatial auto-correlation denoted by Moran's I (i.e., spatially variable cell types, as detailed in Fig. 2.b). In other words, on top of the reasonably high performance across all cell types, Hist2Cell achieves even more accurate prediction for cell types that may have specific spatial patterns, which often relate to biological significance [29–31]. Beyond the quantitative assessment, visualization of the predicted cell type abundances in tissue also shows that Hist2Cell accurately identifies spatial patterns of cell type distributions, with fewer false positives compared to other methods, for example in ciliated cells, IgA plasma cells, and SMG Serous cells (Fig. 2.f).

Cell Type Colocalization Patterns. Next, we examined the pair-wise colocalization among these 80 cell types by performing a spatial correlation with bi-variant Moran's R as implemented in SpatialDM [26]. Briefly, this statistic calculates the correlation between the abundances of two cell types while considering spatial auto-correlation. Overall, we found that the patterns of colocalization among these 80 cell types are highly consistent between the quantified abundance from ST and predicted ones from histology by our Hist2Cell (Fig.2.e). By contrast, discordance is evident if using the cell type abundance predicted by the counterpart method STNet. As a prominent example, Hist2Cell identifies colocalization between IgA plasma cells and submucosal glands (SMGs) in human airways, which is one of the major discoveries in the original study [24]. Impressively, with the observed cell type abundance from ST, IgA plasma was only ranked as the 7th colocalized cell type for SMGs, while IgA plasma was ranked the 1st for SMGs' colocalized

partner if using predicted cell type abundance by our method (Fig.2.f). These results suggest that the global colocalization patterns and the individual cell type pairs with critical interaction can be identified by our method, by only using histology images. Detailed cluster maps can be found in Supplementary Fig. 6 to Fig. 8.

Manual Annotation Evaluation By comparing Hist2Cell predictions with manual annotations from the original study [24] of the dataset (Fig 3.a), we conclude that Hist2Cell's outputs can serve as reliable

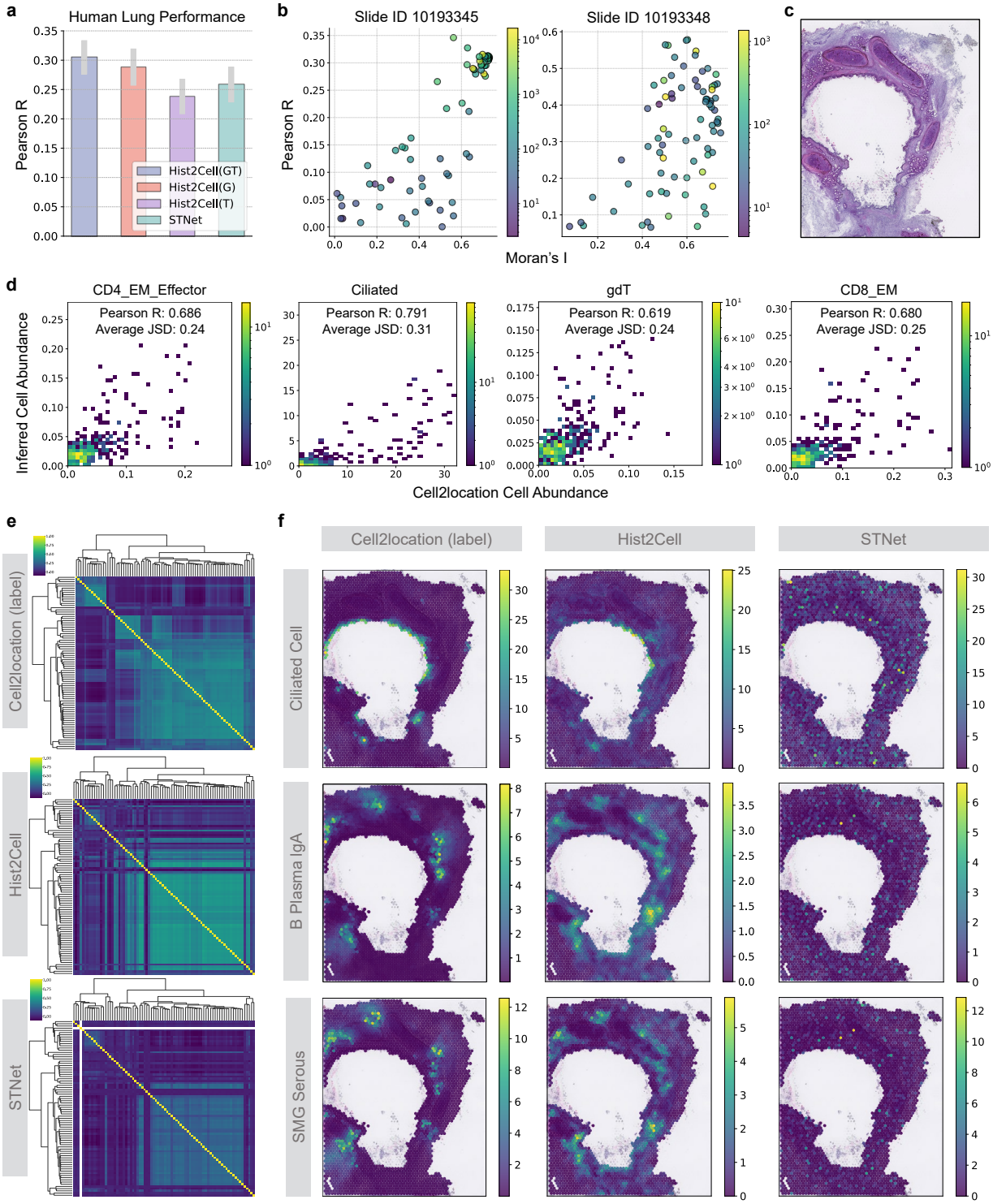

Fig. 2: (Caption next page.)

Fig. 2: **Hist2Cell can map fine-grained human lung cellular architectures. a,** Histogram depicting the average Pearson's R values for cell abundance prediction in the leave-one-donor-out cross-validation experiment conducted on the healthy human lung dataset. Hist2Cell demonstrated more accurate predictions of fine-grained cell type abundances across locations compared to other baselines. **b,** Scatter plot for two test slides illustrating the relationship between spatial auto-correlation (Moran's I; x-axis) and Hist2Cell's prediction performance (y-axis) in the healthy human lung dataset. Hist2Cell excelled in predicting cell types exhibiting higher spatial auto-correlation. **c,** Example H&E image for slide (ID) 9258464. **d,** 2D histogram plots showcasing the concordance of cell abundance between ground truth (x-axis) and Hist2Cell's prediction (y-axis) across all testing spots in the healthy human lung dataset. Color denotes 2D histogram counts. Pearson's R denotes Pearson's correlation coefficient, and JSD denotes Jensen–Shannon divergence. Hist2Cell showed significantly high positive correlations with several key cell types. **e,** Clustermaps colored by the bivariate statistic Moran's R for cell type pairs. Top: results from ground truth cell type abundances estimated from the spatial transcriptomics data using cell2location algorithm. Middle: results from predictions of Hist2CellḂottom: results from predictions of STNet. Hist2Cell provided a more consistent cell-cell colocalization analysis with the ground truth cell abundances. **f** related to (c), the visualizations comparing the spatial cell abundances as determined by ground truth, Hist2Cell, and STNet predictions for select key cell types. Hist2Cell show less false positives than STNet.

references for biological research, such as the discovery of macro and micro-anatomical tissue compartments. Specifically, Hist2Cell's accurately predicted cell types correspond to their known locations, like ciliated epithelial cells in the lumen of the airway surrounded by basal cells, and alveolar types 1 and 2 (AT1 and AT2) cells in lung parenchyma, as shown in Fig 3.b. Furthermore, Hist2Cell accurately localized one fibroblast population, enriched in the airways, to its specific region around the airway epithelium (peribronchial fibroblasts-PB-fibro), as depicted in Fig 3.c. This finding also validates the clinical value of Hist2Cell, as PB-fibro is recognized as a key cell type in lung disease [24]. In the Supplementary Fig. 4, we also compare the predictions of STNet with the manual annotation, which shows poor alignments between the cell types and the tissue compartments.

2.2 Hist2Cell can Generalize to External Breast Cancer Samples

To evaluate the generalizability and clinical applications of Hist2Cell, we conducted an external validation experiment using human breast cancer tissues. Specifically, the Hist2Cell model was trained on the her2st breast cancer dataset (13,620 spots in 36 sections from 8 patients) [25] to predict cell abundance for 39 cell types and was then directly applied to the STNet breast cancer dataset (30,655 spots in 69 sections from 23 patients) [17] without any re-training. All performance comparisons, visualizations, and analyses are reported using the external STNet dataset. More details about the 39 cell types can be found in the Supplementary Fig. 2.

The overall Pearson correlations on the external dataset revealed that Hist2Cell provides more accurate predictions of cell type abundances across various locations compared to other methods and their variants (see Fig.4.a). Specifically, on the external dataset, Hist2Cell's predictions positively correlated with all 39 cell types across all samples, exhibiting an average Pearson's correlation of 0.28. On the contrary, STNet only has an average Pearson's correlation of 0.23 on the external dataset. This suggests that Hist2Cell possesses superior generalization capabilities (21% performance increase to STNet) on external data despite technical differences in sample preparation and imaging techniques of different datasets. The favorable generalization of Hist2Cell might be attributed to its model architecture and the random subgraph sampling strategy. The model architecture integrates both local and global correlations within tissue slides, facilitating the learning of more robust histological image representations. Additionally, the random subgraph sampling strategy preserves data diversity throughout the training process. Moreover, Hist2Cell maintains significantly high positive correlations with several key cell types on the external dataset (Pearson's R>0.68; Fig. 4.c), such as fibroblast as a common component in the tumor microenvironment of breast cancer [32], luminal epithelial cells of the mammary gland that can produce basal cells upon oncogenic stress [33], lgA plasma cells as the major player of the tumor-immune interaction [34], and vascular-associated smooth muscle cells.

Hist2Cell also achieves elevated accuracy in predicting spatially variable cell types (i.e., higher Moran's I; Fig. 4.b) on the external dataset, corroborating findings from the human lung dataset. Beyond quantitative assessment, the ability of Hist2Cell and other methods to accurately identify locations with conspicuously

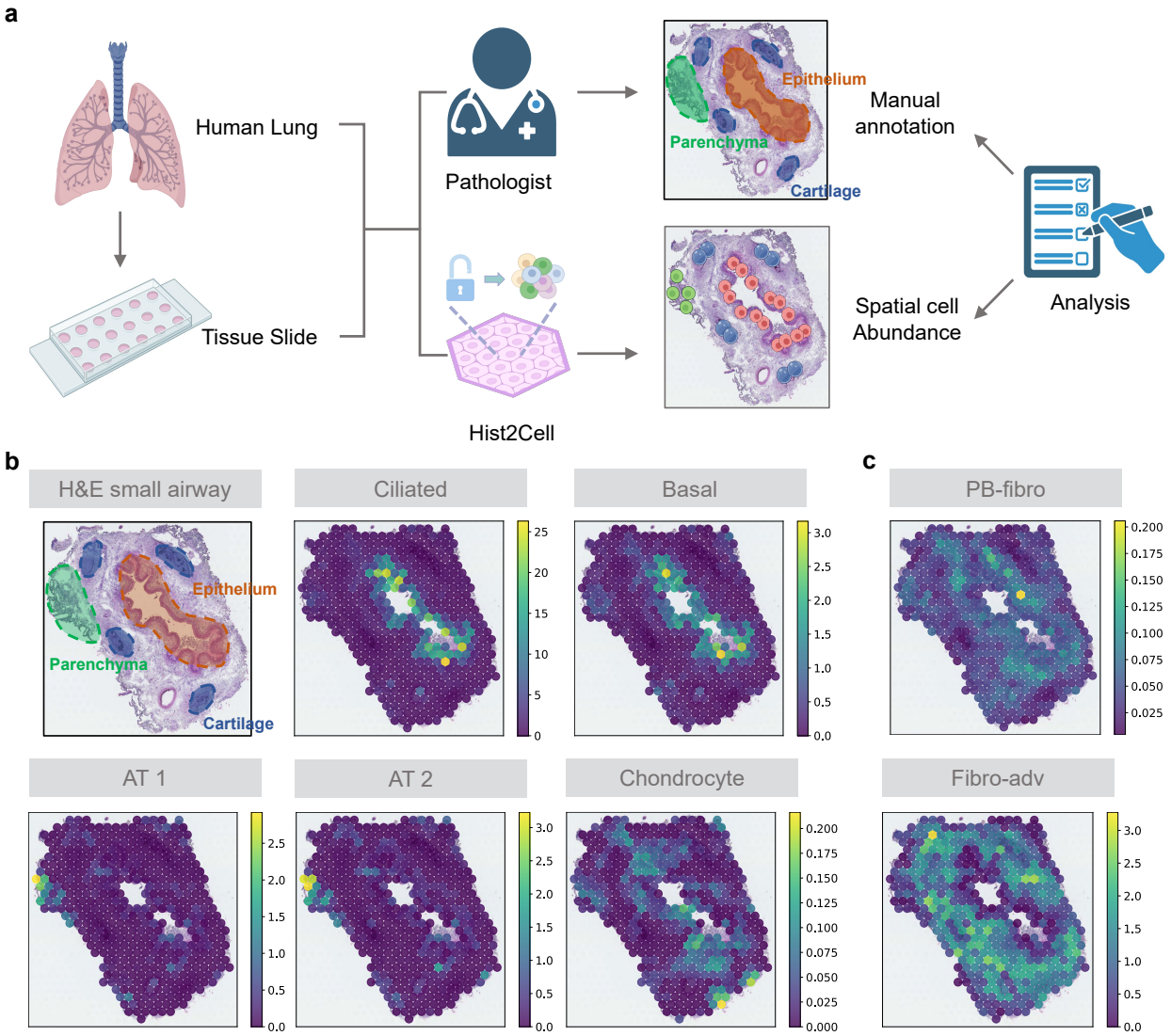

Fig. 3: **a,** Analysis workflow incoporating Hist2Cell and manual annotation. **b,** Mapping with Hist2Cell on Visium ST of a bronchi section demonstrates the alignment of cell types with their expected anatomical structures. H&E staining and cell abundance predictions by Hist2Cell (denoted as density scores) for ciliated, basal epithelium, AT1, AT2, and chondrocyte cell types are overlaid on a histology image. Dotted lines demarcate the epithelium (pink), parenchyma (green), and cartilage (brown). **c,** Cell abundance predictions by Hist2Cell indicate that PB-fibro cells localize around the airway epithelium.

high cell abundance of specific cell types was also evaluated on the external dataset. Visualizations in Fig. 4.e demonstrate that Hist2Cell accurately identifies the presence of cell types such as IgA plasma cells, CD4-positive helper T cells, and luminal epithelial cells of the mammary gland, with fewer false positives than other methods on the external dataset. When comparing these visualizations with manual pathology tumor/normal annotations (Fig. 4.c), it was observed that the inferred cellular architectures closely match human expert annotations, showing the capability of capturing intratumor heterogeneity of Hist2Cell.

Furthermore, we assess if Hist2Cell can effectively identify colocalization among these fine-grained cell types on the external dataset. Similar to the human lung data, we used the bi-variate Moran's R statistic to calculate the spatial correlation and analysis of the cluster maps on this value. Fig.4.b indicates that Hist2Cell outperforms the other method, showing a global pattern more akin to that obtained from the probed ST by cell2location. As a notable example, the colocalization between effector memory CD8-positive, alpha-beta T cell with myeloid dendritic cell is a highly ranked interacting pair (Moran's R=0.38). By directly predicting from histology, Hist2Cell also identifies the high spatial correlation between these two cell

types (Moran's R=0.26), confirming the complex cooperation among immune cells against tumor cells [35]. Specifically, with the observed cell type abundance from ST, effector memory CD8-positive, alpha-beta T cell was ranked as the 1st colocalized cell type for myeloid dendritic cell, and it is ranked as the 2nd colocalized cell type if using predicted cell type abundance by our method (Fig. 4.e). Detailed cluster maps can be found in Supplementary Fig. 9 to Fig. 11. Taken together these results suggest that the predictions from Hist2Cell uncover promising colocalization patterns despite batch effect and technique difference, potentially

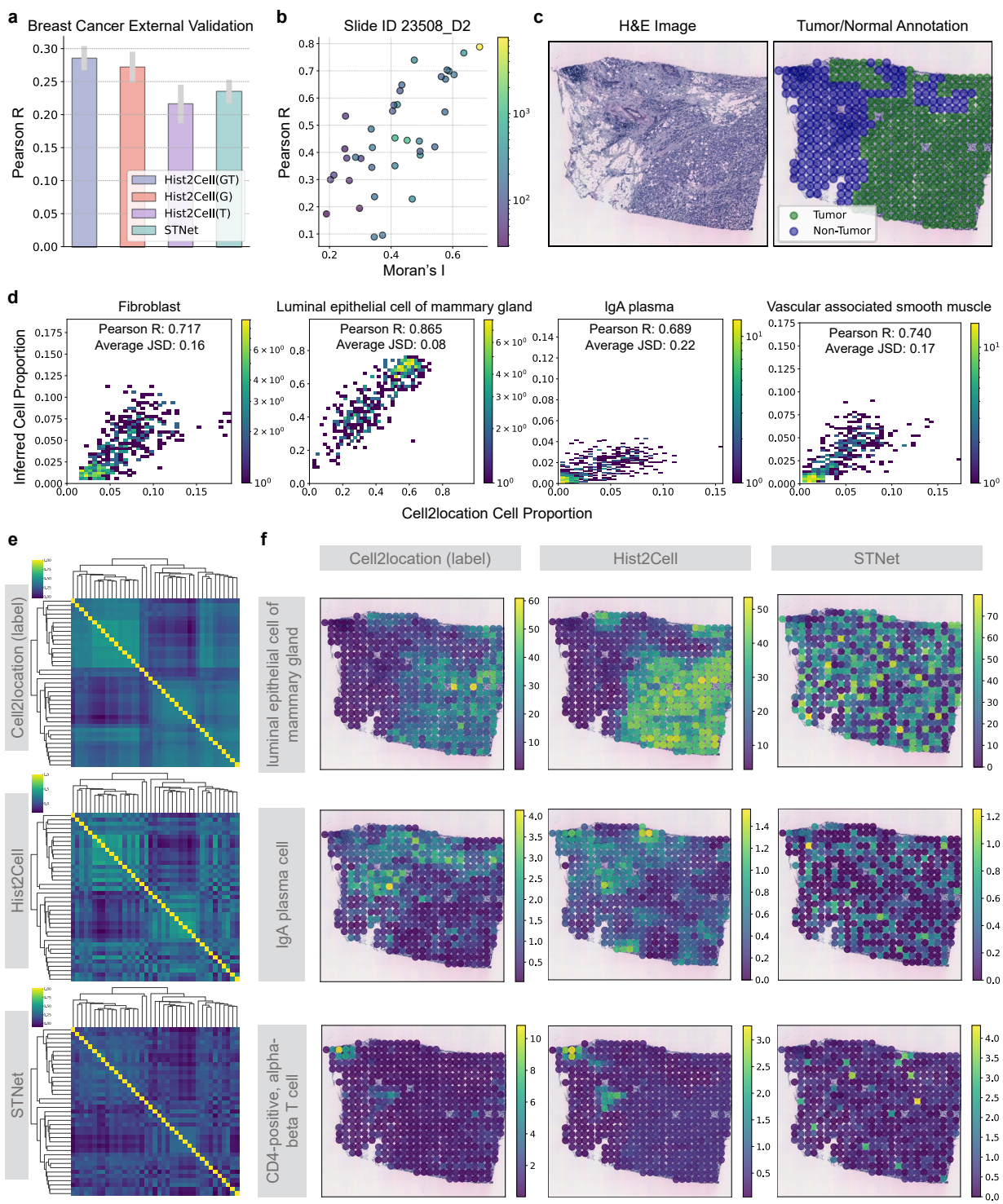

Fig. 4: (Caption next page.)

Fig. 4: **Hist2Cell can generalize to external breast cancer samples. a,** A histogram representing the average Pearson's R values for cell abundance prediction in the external breast cancer dataset. Hist2Cell demonstrated superior accuracy and generalizability in predicting fine-grained cell type abundances across different locations compared to other baseline models. **b,** A scatter plot for one test slide illustrating the relationship between spatial auto-correlation (x-axis) and Hist2Cell's prediction performance (y-axis) in the external breast cancer dataset. Hist2Cell excelled in predicting cell types with higher spatial auto-correlation. **d,** 2D histogram plots showcasing the agreement between the ground truth cell abundance (x-axis) and that predicted by Hist2Cell (y-axis) across all testing spots in the external breast cancer dataset. **e,** Clustermaps colored by the bivariate statistic Moran's R for various cell type pairs. The top shows results from ground truth cell type abundances estimated from spatial transcriptomics data using the cell2location algorithm. The middle displays results from predictions by Hist2Cell. The bottom presents results from predictions by STNet. Hist2Cell provided more consistent cell colocalization patterns compared to the ground truth cell abundances. **c,f** H&E images, manual tumor/normal annotations of slide (ID) 23508D2, and visualizations comparing the spatial cell abundances as determined by ground truth, Hist2Cell and STNet for certain key cell types. Hist2Cell showed fewer false positives compared to STNet.

facilitating the discovery of context-specific cellular cooperation and signaling on external datasets, which is crucial for its research and clinical usage.

2.3 Hist2Cell Enables Consensus Cellular Analysis from Large-scale H&E Cohorts

As Hist2Cell generalizes well on external breast cancer samples, we incorporate large-scale breast cancer histology slide datasets from the TCGA repository and adopt Hist2Cell to provide consensus cellular analysis, as shown in Fig.5.a. It is worth noting that there were several notable differences between the TCGA and training breast cancer data. The TCGA slides are collected and scanned at different institutions and only have bulk RNA-seq data that is not conducted on the same tissues used for imaging, which poses a substantial challenge for fine-grained cellular analysis. We applied Hist2Cell directly to H&E slides of 565 TCGA breast tumor samples from 565 patients without any model re-training.

To quantitatively evaluate the predictions of Hist2Cell, we first estimate the bulk cell abundance of each sample according to their bulk RNA-seq with cell2location. The predictions of Hist2Cell were averaged into a pseudo-bulk cell abundance profile for each sample. For all samples in the large cohort, the predicted pseudo-bulk cell abundance profile correlated positively with 26 of 39 cell types. The correlation was significantly positive for 13 cell types (FDR lower than 0.05). Among them, fibroblast cells have the highest positive correlation as shown in Fig. 5.b, with an average Jason-Shannon Divergence of 0.26 among all 565 TCGA breast cancer slides. We also noticed that Hist2Cell excelled in predicting cell types with higher bulk cell abundance (Fig.5.c), which were generally more significant in tumor analysis. For instance, in Fig.5.c, Hist2Cell shows better predictions for cell types including fibroblast, luminal epithelial cell of the mammary gland, and naive B cell, which is consistent with the findings in the previous section.

More importantly, by aggregating the cellular architectures from hundreds of patients, Hist2Cell unleashes the remarkable potential of large-scale public H&E cohort and is capable of providing consensus and robust analysis for cell-cell communication analysis for biological research. As shown in Fig.5.d, Hist2Cell identified cell pairs with both high average Moran's R statistic and high cell pair density (product of bulk cell abundances) among all 565 breast cancer samples. We further investigated recurrence patterns, as depicted in Fig.5.e, by visualizing cell type colocalization relationships characterized by both high average Moran's R values and a significant number of slides with high Moran's R (greater than 0.20). Specifically, we highlighted those relationships where the number of slides with high Moran's R exceeded 470. Also, we show the detailed cell type colocalization analysis provided by Hist2Cell in Fig.5.f. Among them, the colocalization of T cells with myeloid cells can still be observed in the consensus setting (Moran's R with T cell ranked 3rd for myeloid cell), which is consistent with the findings in previous study [25]. In addition, Hist2Cell inferred cell abundances had the power to distinguish normal/tumour regions of breast cancer tissues from TCGA as shown in Fig.5.g. Moreover, we explore the impact of large-scale studies on the analytical power of Hist2Cell. As depicted in Supplementary Fig 5, we visualized the cell type colocalization analysis performed by Hist2Cell across various sample sizes. Specifically, n denotes the number of randomly sampled slides from the TCGA breast cancer cohort. Using n values of $1, 2, 4, \ldots, 128$, and the entire cohort,

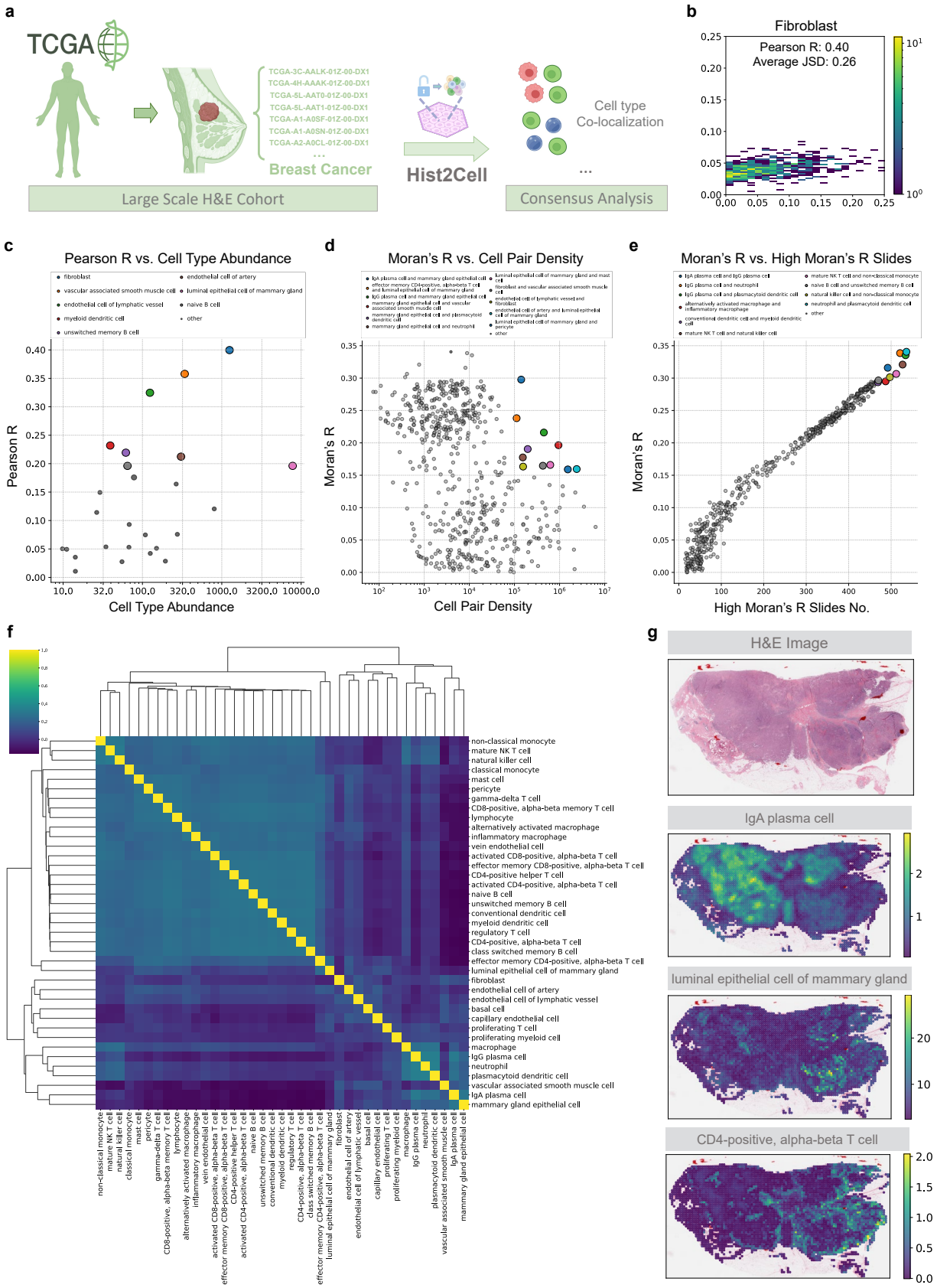

Fig. 5: (Caption next page.)

Fig. 5: **Hist2Cell can provide consensus analysis from large-scale H&E TCGA Cohorts. a,** An illustration of the large-scale study process using Hist2Cell on TCGA breast cancer cohorts, demonstrating how consensus cellular analysis can be achieved from data spanning hundreds of patients. **b,** 2D histogram plots showing the concordance between the ground truth cell proportion (x-axis) and the cell proportion predicted by Hist2Cell (y-axis) for fibroblast cells across all cases in the TCGA breast cancer cohort. **c,** A scatter plot illustrating the relationship between cell abundance (x-axis) and Hist2Cell's prediction performance (y-axis) across all cases in the TCGA breast cancer cohort. Hist2Cell excelled in predicting cell types with higher abundances. **d,** A scatter plot showing the relationship between cell pair density (x-axis) and the average bivariate statistic Moran's R as calculated by Hist2Cell (y-axis) among all cases in the TCGA breast cancer cohort. Hist2Cell effectively distinguished cell pair colocalization when the density of the cell pairs was high. **e,** A scatter plot illustrating the relationship between the number of slides with high Moran's R values (x-axis, Moran's R greater than 0.20) and the average bivariate statistic Moran's R as calculated by Hist2Cell (y-axis) for all cases in the TCGA breast cancer cohort. Highlighted points represent colocalization patterns Hist2Cell identified among most slides of the entire cohort. **f,** Consensus clustermaps colored by the average bivariate statistic Moran's R, calculated from Hist2Cell's predictions for cell type pairs across all cases in the TCGA breast cancer cohort. **g,** H&E images, and visualizations of spatial cell abundance predictions by Hist2Cell for a slide in the TCGA breast cancer cohort. Hist2Cell's inferred cell abundances effectively differentiated between normal and tumor regions in breast cancer tissue.

we generated consensus clustermaps based on Hist2Cell's predictions. It was observed that the patterns of cell type colocalization gradually stabilized as the number of slides increased, indicating that more reliable analysis can be achieved with larger sample sizes. These analyses suggest that Hist2Cell can generalize to large-scale public H&E cohorts despite the technical differences in the samples and imaging techniques, and thus provide consensus cellular analysis for biologists.

2.4 Hist2Cell can Provide Super-resolved Fine-grained Cellular Maps

Hist2Cell, leveraging its scalability enabled by subgraph sampling, excels in inferring super-resolved cell abundance maps. As illustrated in Fig.6.a, by sampling subgraphs from higher-resolution spot coordinates, Hist2Cell is capable of providing super-resolved cellular maps by either imputing (fine-tuning) on lower-resolution cellular maps or directly predicting from histology images with its pre-trained parameters. To assess Hist2Cell's proficiency in resolving higher resolution cell abundance maps, we inferred 2× cell abundance for a sample in the human lung dataset, as shown in Fig.6.b. It was observed that both imputation-based and prediction-based super-resolved cellular maps provide a more detailed mapping in relation to different tissue structures in concordance with the manual annotations in Fig.3.a. In Supplementary Fig. 3, we further show the super-resolved cellular maps of human breast cancer tissue, which also demonstrate a more fine-grained boundary consistent with the tumor/normal annotations in Fig 4.c. We observe that imputation-based maps are more consistent with the lower-resolution cellular maps, while prediction-based maps exhibit more concentrated cellular clustering patterns based on the morphological features of the histology images. Although some prior studies have focused on super-resolving low-resolution Spatial Transcriptomics (ST) data [12, 14], we highlight that Hist2Cell is uniquely capable of directly providing super-resolved cellular maps from histology images. Specifically, Hist2Cell can offer super-resolved cellular maps even when low-resolution spatial cell abundances are unavailable, by utilizing the knowledge embedded in its pre-trained parameters. This unique capability renders super-resolved cellular mapping applicable to the vast array of H&E images routinely utilized in clinical settings. In summary, Hist2Cell provides a cost-effective method for achieving cell abundance super-resolution, enabling the acquisition of high-resolution cellular maps directly from histology images.

3 Discussion

In this work, we have presented Hist2Cell, a Graph-Transformer framework that decodes fine-grained cellular architectures from tissue morphological features with haematoxylin-and-eosin-stained histology image inputs. We demonstrate that the knowledge within spatial transcriptomics and single-cell sequence signatures can be well captured by our deep learning method, and thus transferred to readily available H&E

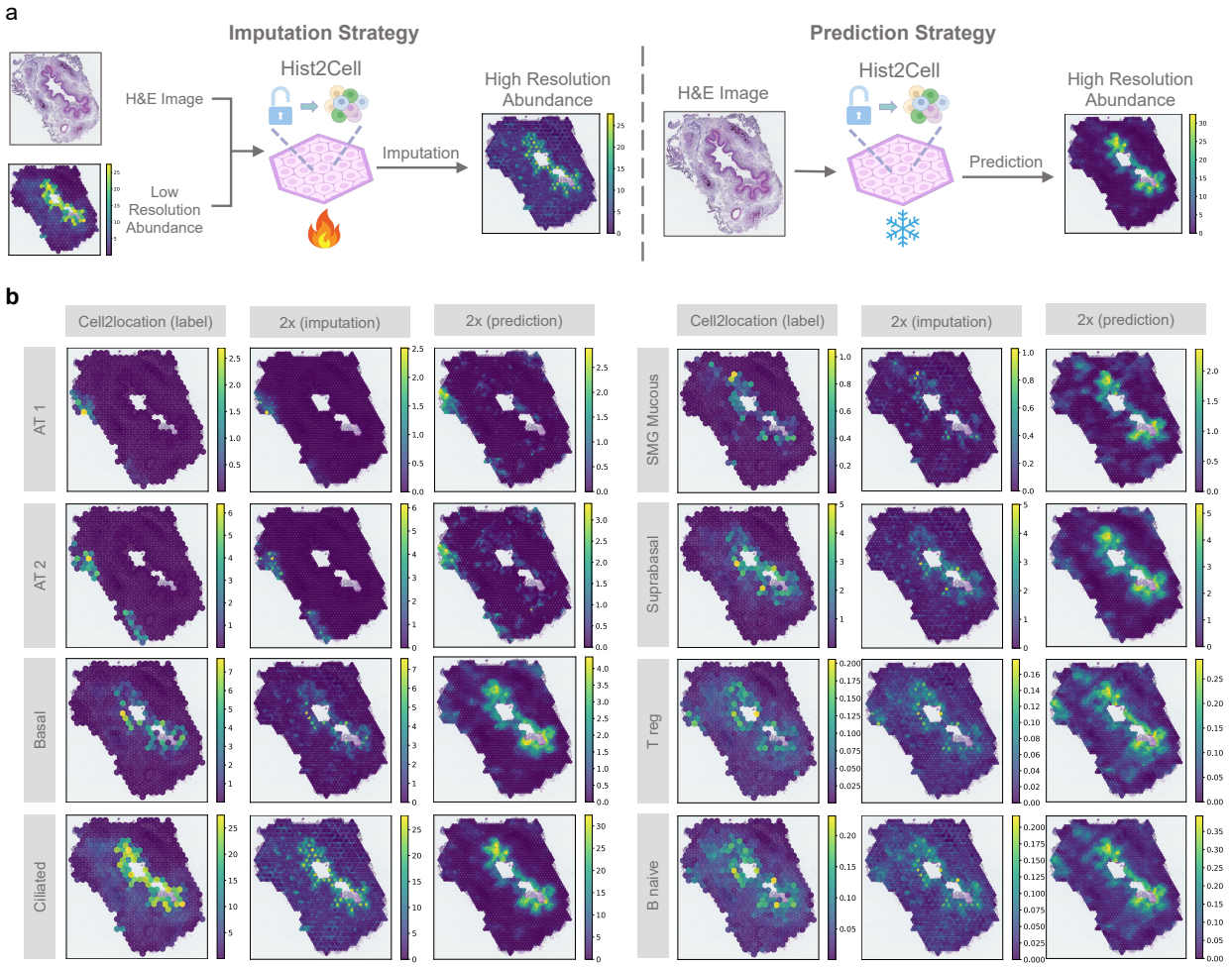

Fig. 6: **Hist2Cell can provide super-resolved fine-grained cellular maps. a,** An illustration of the two super-resolution strategies based on Hist2Cell. Left: Hist2Cell can impute from low-resolution cellular maps by fine-tuning its pre-trained parameters. Right: Hist2Cellcan also directly predict high-resolution cellular maps with its pre-trained parameters frozen. **b,** Visualizations comparing low-resolution ground truth cell abundance with both imputed and directly predicted high-resolution results by Hist2Cell. Both approaches provide a more detailed mapping in concordance with the manual annotation shown in Fig. 3.a, highlighting different tissue structures.

histology images to provide fine-grained cellular maps. Hist2Cell produces accurate predictions for held-out donors in human lung tissues. Moreover, it can generalize to external datasets despite batch effect and technique differences of imaging without any re-training, as evident by the breast cancer datasets. We also find that Hist2Cell can capture cell abundance heterogeneity within tumours and different tissue structures. Although this paper focuses on human health lung and breast cancers, the technical framework of Hist2Cell can be broadly applied to other tissue types.

In addition to predicting and identifying single cell type abundance, the prediction of Hist2Cell can also be used for analysing cell colocalization patterns. For example, it reveals the cell type colocalizations in the airway cartilage of human lungs. We also find it promising that Hist2Cell can make predictions of public large-scale H&E corhorts without any model re-training, despite the substantial differences in the data. This opens the door to apply Hist2Cell to large existing cohorts of histology images and provide consensus biology research analysis, such as inferring important bio-markers like cell-cell communication within important tissue sections such as tumor areas. Moreover, due to the scalable nature of the designed framework, Hist2Cell can also infer higher resolution cell abundance maps than the current spatial transcriptome technique.

Hist2Cell demonstrates that spatially resolved cell abundances of biology interest can be directly inferred from tissue images. Although other machine-learning approaches can identify coarse-grained cell types (e.g.,

6 cell types) from whole histology slides [18], Hist2Cell can decode much more complex cell architectures in a more fine-grained manner (up to 80 different cell types) by learning from spatial transcriptomics as well as single-cell sequence signatures. Our proof-of-concept study finds that the combination of spatial transcriptomic, single-cell sequence and deep learning can provide direct fine-grained cellular architecture identification solely from histology images, allowing further study of complex cell interactions and variations.

Hist2Cell can potentially enable new image-based screens of cellular biomarkers demonstrating spatial variation and association from large public H&E cohorts, which opens an exciting new direction for clinical applications. As different tissues contain an intersection of fine-grained cell types and share similar morphological features, an interesting direction for future work would be to explore the commonalities and differences among different spatial transcriptome datasets for building a foundation model for pan-cancer analysis.

4 Methods

4.1 Data Description

The dataset comprising healthy human lung samples was obtained and processed as described in a prior study [24]. This dataset includes 11 slices from tissue sections encompassing the human trachea, bronchi, and both upper and lower parenchyma from 4 patients, totaling 20,770 spots. Visium Spatial Transcriptomics (ST) at 10× magnification was conducted on these slices, and Hematoxylin and Eosin (H&E) images produced during the Visium protocol were captured at a ×20 magnification. The study identified 80 fine-grained cell types and estimated their absolute spatial abundances in the Visium ST data using the cell2location method (version 0.1) [8]. The her2st dataset [25] comprised HER2-positive breast tumors from 8 individuals (Patients A-H). From each individual, either 3 adjacent or 6 evenly spaced sections were obtained (totaling $n = 36$ sections), which were then subjected to Spatial Transcriptomics (ST) [36]. In total, this dataset encompasses 13,620 spots, each with corresponding spatial transcriptomics data. For imaging, the her2st dataset was analyzed using the Metafer VSlide system at ×20 magnification. The STNet dataset [17] included samples from 23 breast cancer patients. For each patient, the dataset contained three microscope images of slides with H&E-stained tissues and their corresponding spatial transcriptomics data, comprising a total of 30,655 spots. The biopsies were collected and processed in accordance with the methods outlined in previous work [36]. Our large-scale study section utilized 565 slides from 565 breast cancer patients, sourced from The Cancer Genome Atlas (TCGA) repository. In line with the approach of previous studies [17], although the bulk RNA-seq for each patient was not performed on the same tissue as the H&E-stained slides, it was utilized as the representative average RNA-seq data for each slide.

4.2 Data Preprocessing

Spatial Mapping of Cell Types for Breast Cancer Datasets We employed the fine-grained spatial cell abundance, as estimated from spatial transcriptomics data, as ground truth for training and evaluating Hist2Cell. To maintain consistency with the healthy human lung dataset, we utilized the cell2location method to estimate the fine-grained spatial and bulk cell abundances for the her2st, STNet, and TCGA datasets, respectively. The scRNA-seq data from the Human Breast Cell Atlas (HBCA) [37] served as the reference for gene expression signatures of various cell types. This single-cell transcriptomics dataset profiles 714,331 cells from 126 women, uncovering abundant pericyte, endothelial, and immune cell populations, alongside a wide diversity of luminal epithelial cell states. This makes it an excellent reference for studying mammary biology and breast cancer pathology. Specifically, this dataset offers annotations for 39 distinct cell types, encompassing both breast cancer ($n = 144,285$) and normal breast cells ($n = 570,046$).

H&E Image Preprocessing For the healthy human lung, her2st, and STNet datasets, we cropped 224×224 image patches from the whole-slide images. These patches were centered on the spatial transcriptomics spots to predict the fine-grained cell type abundances for each spot. For the breast cancer slides from the TCGA repository, we processed the whole-slide images into patches containing substantial tissue amounts, adhering to the pipeline established in previous studies [38]. Initially, candidate 224×224 patches were cropped from the whole-slide images without overlap, under a ×10 magnification. Subsequently, patches predominantly consisting of background were discarded. A pixel within a patch was classified as background if its mean RGB value was less than or equal to 220 (indicating a color close to white). A patch was excluded if over 75% of its pixels were categorized as background. Each selected patch was treated as one spot in the TCGA

slides. The central pixel coordinates of each spot were utilized for graph construction, visualization, and downstream analysis in our study.

4.3 Hist2Cell Design and Training

Hist2Cell is constructed by leveraging the advantages and addressing the limitations of previous works focused on predicting gene expression from histology images, incorporating their key findings. Current approaches can be divided into two groups: (1) global-based methods and (2) local-based methods. In global-based methods, the core concept involves using Whole Slide Images (WSIs) to simultaneously predict an expression map for all coordinates. This enables the model to consider spatial associations between spots. However, this method suffers from severe data scarcity, making models prone to overfitting. Additionally, processing the entire WSI incurs in a high computational cost. Conversely, local-based methods rely solely on the visual information available at each coordinate for predicting gene expression. Training on spot patches, local-based methods benefit from abundant data for deep learning training. Nevertheless, such methods do not take into consideration characteristics such as the vicinity of the patch or long-range interactions, resulting in sub-optimal performance. Previous studies have also discovered that images with similar features tend to exhibit similar gene expression patterns, regardless of their location within the tissue [39, 40]. Building on these findings, we propose employing k-hop subgraphs as the fundamental unit of our framework and utilize a Graph-Transformer architecture to learn both local context and distant relations, thus benefiting from the advantages of local-based and global-based methods without succumbing to their respective limitations.

To be specific, the key idea of our approach is to execute a minibatch of local subgraphs sampled from a WSI instead of using an entire WSI as a single data element. This strategy conserves computational resources and mitigates the overfitting risks commonly associated with using large WSIs, which makes our framework suitable for super-resolved cellular maps inference and improves the generalization of our framework. To better model the relationships within each subgraph and among different subgraphs, we employed a Graph-Transformer architecture. The Graph Attention layers facilitate message passing between spots and their spatial neighbors, learning the local spatial context within each subgraph, while the Transformer layers calculate the attention score among any pair of spots despite the physical distance, modeling long-range correlations existing among different subgraphs. Details are illustrated in the subsequent sections.

4.3.1 Spatial Graph Construction

As illustrated in Fig. 1b, we abstract the whole-slide image (WSI) into a spatial graph. Within this spatial graph, each node corresponds to a 224×224 image patch, centered on specific spatial spots, targeted for spatial cell abundance prediction. Utilizing the spatial coordinate information of all nodes, we calculate the distances between nodes using the Euclidean distance. For each node, we select k nearest nodes based on the smallest Euclidean distances, where $k = 6$ for $10\times$ Visium data and $k = 8$ for ST data [36]. Leveraging the spatial neighbor relationships, we construct an undirected graph, denoted as $G = \{V, E\}$, to represent the corresponding whole-slide image. Here, the node set V represents the image patches, and the edge set E indicates the spatial neighbor relationships among these patches.

4.3.2 Local Subgraph Sampling and Embedding

The core concept involves initially sampling all the nodes required for computation. We begin by randomly sampling a minibatch of central nodes, denoted as B, from the spatial graph G. Subsequently, using a pre-defined radius k for local subgraphs, we gather all necessary nodes for computation, denoted as $B^k = B \cup N_1(B) \ldots \cup N_k(B)$. We use the notation $N_i(B)$ to denote a deterministic function which specifies the set of all i-hop neighbor nodes of all center nodes in B. In this study, we use $k = 2$ for both training and inference of Hist2Cell. Together with B^k, we obtain the spatial neighbor relationship E_B^k among all nodes in B^k as the corresponding subset of edge set E. To embed the image patches within B^k, we employ a feature extractor, represented as $I(\cdot)$, to learn fine-grained spatial heterogeneity in cell type abundances within the tissue. This yields a low-dimensional embedding $I_{\text{emb}} \in \mathbb{R}^{\left[d_{\text{emb}}, |B^k|\right]}$, where d_{emb} is the dimension of extracted node embedding, and I_{emb} denotes all node embedding of B^k. In our experiments, we used a ResNet-18 [41] model with pre-trained ImageNet [42] weights as its initialization. The ResNet-18 model comprises 18 convolutional layers with residual connections, followed by a fully connected layer. We remove the fully

connected layer and use the feature embedding before it as the node embedding in our study. Throughout the training of Hist2Cell, the parameters of the ResNet-18 model are optimized in an end-to-end fashion.

4.3.3 Short-range Local Message Aggregation

Adhering to the principles of the Graph-Transformer architecture, Hist2Cell initially employs a Graph Attention layer to learn local representations of sampled subgraphs B^k. As demonstrated in prior studies [43, 44], the Graph Neural Network (GNN) component of a Graph-Transformer architecture derives node representations from neighborhood features. This neighborhood aggregation in GNN plays a crucial role in learning local and short-range correlations among graph nodes. Specifically, we implement the GATv2 layer [45] for message propagation and aggregation. The message propagation and aggregation of node i in B^k are defined as:

$$\boldsymbol{h}_i' = f_\theta\left(\boldsymbol{h}_i\ , \text{Aggregate}\left(\{\boldsymbol{h}_j \mid j \in N_i\}\right)\right) = \sigma\left(\sum_{j \in N_i} \alpha_{ij} \cdot \boldsymbol{W}\boldsymbol{h}_j\right), \tag{1}$$

where h_i and h_j are the node embeddings of node i and node j from the previous layer, and N_i denotes the set of all spatial neighbor nodes of node i in B^k. Thus, the GATv2 layer computes a weighted average of the transformed features of neighbor nodes (followed by a nonlinearity σ) as the new representation $\boldsymbol{h}_i'$ of node i, using normalized attention coefficients α_{ij}. For attention coefficient calculation, a scoring function $e : \mathbb{R}^{d_{\text{emb}}} \times \mathbb{R}^{d_{\text{emb}}} \to \mathbb{R}$ computes scores for each edge (j, i), indicating the importance of neighbor node j's features to node i:

$$e\left(\boldsymbol{h}_i, \boldsymbol{h}_j\right) = \boldsymbol{a}^\top \text{LeakyReLU}\left(\boldsymbol{W} \cdot [\boldsymbol{h}_i \| \boldsymbol{h}_j]\right), \tag{2}$$

where $\boldsymbol{a} \in \mathbb{R}^{2d'}$, $\boldsymbol{W} \in \mathbb{R}^{d' \times d}$ are learned during the training process, and $\|$ denotes vector concatenation. The attention scores are normalized across all neighboring nodes in N_i using the softmax function, and the attention function is defined as:

$$\alpha_{ij} = \text{softmax}_j\left(e\left(\boldsymbol{h}_i, \boldsymbol{h}_j\right)\right) = \frac{\exp\left(e\left(\boldsymbol{h}_i, \boldsymbol{h}_j\right)\right)}{\sum_{j' \in N_i} \exp\left(e\left(\boldsymbol{h}_i, \boldsymbol{h}_{j'}\right)\right)}. \tag{3}$$

4.3.4 Long-range Global Correlation Learning

In Hist2Cell, apart from the local aggregation of neighbor nodes, we also learn the long-range correlations among all sampled nodes in B^k. The underlying premise is that spots exhibiting similar morphological features should have similar cell abundances, regardless of their distance within the tissue. Hist2Cell employs the Transformer [46] to learn these long-range correlations, treating each node in B^k as tokens. The core component of the Transformer is its multi-head attention mechanism, denoted as:

$$\text{MultiHead}(Q, K, V) = [O_1, \ldots, O_{head}]\, W^O, \tag{4}$$

$$O_i = \text{Attention}\left(QW_i^Q, KW_i^K, VW_i^V\right) = \sigma\left(\boldsymbol{Q}\boldsymbol{K}^T\right)\boldsymbol{V}. \tag{5}$$

Within this formula, *head* represents the number of parallel attention layers, and σ denotes an activation function. Utilizing the components mentioned above, the Transformer layer is defined as:

$$Z = \text{LayerNorm}\left(H_{\text{L}} + \text{MultiHead}\left(H_{\text{L}}, H_{\text{L}}, H_{\text{L}}\right)\right), \tag{6}$$

$$\hat{H}_{\text{L}} = \text{LayerNorm}(Z + \text{rFF}(Z)), \tag{7}$$

where H_{L} is the features of B^k fed into the L-th Transformer layer, rFF is a row-wise feedforward layer, LayerNorm is layer normalization [47], and $\hat{H}_j$ represents the transformed features of all spots in B^k after considering the long-range correlations.

4.3.5 Multi-scale Feature Fusion and Prediction

In the final stage, Hist2Cell fuses multi-scale features from the feature extractor, the Graph Attention layers, and the Transformer layers using a residual block as shown in Fig.1b, which can be denoted as:

$$X_{fuse} = w_i I_{\text{fuse}} + w_g X_{GAT} + w_t X_{Trans}, \tag{8}$$

where X_{fuse}, I_{fuse}, X_{GAT}, and X_{Trans} are the fused features, features from the feature extractor, Graph Attention part, and Transformer part, respectively, and w_i, w_g, and w_t are pre-defined weights for feature fusion. Subsequently, we apply Multi-Layer Perceptron (MLP) heads to each node in B^k for spatial cell abundance prediction:

$$\hat{Y} = \text{MLP}\left(X_{fuse}\right). \tag{9}$$

The Mean Squared Error (MSE) loss is employed to optimize the parameters in Hist2Cell using gradient descent. As the training of Hist2Cellis conducted on randomly sampled subgraphs, and the loss term is calculated among all sampled nodes in B^k, the inference phase is slightly different for Hist2Cell. During inference, every spot in the whole-slide image is sampled as the center node of subgraphs. For more reliable cell abundance prediction, we only use the predictions from the center nodes of the subgraphs and merge them into slide-level spatial cell abundances.

4.4 Cell-cell Colocalization Analysis via Spatial Correlation

Cell-cell colocalization analysis, leveraging spatial cell abundance data, was conducted using the spatial correlation statistic, bivariate Moran's R, as implemented in the SpatialDM toolbox [26]. Specifically, to evaluate the spatial correlation between cell type pairs, we calculated the bivariate Moran's R statistic using SpatialDM. The bivariate Moran's R statistic, originally proposed for detecting ligand-receptor pairs exhibiting significant spatial co-expression, facilitates reliable analysis of cell-cell communication in spatial transcriptomics data. This statistic is an extension of techniques previously utilized in geography [48]. Utilizing the available spatial abundance data for various cell types in our study, we directly calculated the bivariate Moran's R statistic between different pairs of cell types. Specifically, the statistic is defined as:

$$\text{Global Moran's } R = \frac{\sum_i \sum_j w_{ij}\left(x_i - \bar{x}\right)\left(y_j - \bar{y}\right)}{\sqrt{\sum_i \left(x_i - \bar{x}\right)^2}\sqrt{\sum_i \left(y_i - \bar{y}\right)^2}}, \tag{10}$$

where x_i and y_j denote the cell abundances of cell types x and y at spots i and j, respectively. The spatial weight matrix computation employs a Radial Basis Function (RBF) kernel with element-wise normalization:

$$w_{ij}^{(0)} = \exp\left\{-\frac{d_{ij}^2}{2l^2}\right\}, w_{ij} = \frac{n}{W} w_{ij}^{(0)}, \tag{11}$$

where d_{ij} represents the geographical distance between spots i and j (Euclidean distance on spatial coordinates), W is the sum of $w_{ij}^{(0)}$, and n is the total number of spots. To assess the efficacy of Hist2Cell in predicting spatial cell abundance, we utilized clustermaps colored according to the bivariate Moran's R statistic. These were derived from both the ground truth spatial cell abundances and the predictions made by Hist2Cell and STNet. The pattern similarities between the clustermaps of the ground truth and those generated by Hist2Cell underscore the effectiveness of our method.

4.5 Super-resolved Spatial Cell Abundance

With the trained Hist2Cell, our framework can provide super-resolved spatial cell abundance predictions by abstracting the whole-slide image into a spatial graph with a reduced distances among different spots. As illustrated in Fig.5.a, this can be achieved in two ways.

Impute from Low-resolution Cellular Map Given a low-resolution cellular map as priors, Hist2Cell can be fine-tuned on this map to make predictions on a super-resolved spatial graph derived from the same whole-slide image. This approach yields higher-resolution spatial cell abundances that are consistent with the low-resolution priors.

Predict from H&E Image Furthermore, Hist2Cell can directly predict super-resolved spatial cell abundances from histology images of human lung and breast tissues, using its parameters optimized on these two tissue sections. These predictions could serve as reliable references, given Hist2Cell's strong generalization capabilities on external data.

5 Data Availability

All datasets employed in this study are previously published and publicly accessible. The healthy lung dataset was downloaded from the Github repository at https://5locationslung.cellgeni.sanger.ac.uk/. The her2st dataset was obtained from https://github.com/almaan/her2st. The STNet dataset was sourced from https://data.mendeley.com/datasets/29ntw7sh4r/5. The TCGA dataset was acquired from the Genomic Data Commons Data Portal at https://portal.gdc.cancer.gov/. The scRNA-seq data from the Human Breast Cell Atlas (HBCA) was downloaded from CELLxGENE at https://cellxgene.cziscience.com/collections/4195ab4c-20bd-4cd3-8b3d-65601277e731. Source data for this study are provided alongside this paper.

6 Code Availability

The Hist2Cell source code are available in Github (https://github.com/Weiqin-Zhao/Hist2Cell). We also uploaded all scripts and materials to reproduce all the analyses at the same website.

7 Acknowledgement

This work was partially supported by the Research Grants Council of the Hong Kong SAR, China (Project No. 27206123 and T45-401/22-N) and the Hong Kong Innovation and Technology Fund (Project No. ITS/274/22).

8 Author contributions

LY and YH conceived and supervised the study. WZ implemented the framwork and performed all data analysis, with support from ZL and XH. WZ, LY and YH wrote the manuscript with inputs from all authors.

References

[1] Armingol, E., Officer, A., Harismendy, O., Lewis, N.E.: Deciphering cell–cell interactions and communication from gene expression. Nature Reviews Genetics **22**(2), 71–88 (2021)

[2] Bloemendal, S., Kück, U.: Cell-to-cell communication in plants, animals, and fungi: a comparative review. Naturwissenschaften **100**, 3–19 (2013)

[3] Stickels, R.R., Murray, E., Kumar, P., Li, J., Marshall, J.L., Di Bella, D.J., Arlotta, P., Macosko, E.Z., Chen, F.: Highly sensitive spatial transcriptomics at near-cellular resolution with Slide-seqV2. Nature biotechnology **39**(3), 313–319 (2021)

[4] Chen, A., Liao, S., Cheng, M., Ma, K., Wu, L., Lai, Y., Qiu, X., Yang, J., Xu, J., Hao, S., *et al.*: Spatiotemporal transcriptomic atlas of mouse organogenesis using DNA nanoball-patterned arrays. Cell **185**(10), 1777–1792 (2022)

[5] Stuart, T., Butler, A., Hoffman, P., Hafemeister, C., Papalexi, E., Mauck, W.M., Hao, Y., Stoeckius, M., Smibert, P., Satija, R.: Comprehensive integration of single-cell data. Cell **177**(7), 1888–1902 (2019)

[6] Andersson, A., Bergenstråhle, J., Asp, M., Bergenstråhle, L., Jurek, A., Fernández Navarro, J., Lundeberg, J.: Single-cell and spatial transcriptomics enables probabilistic inference of cell type topography. Communications biology **3**(1), 565 (2020)

[7] Cable, D.M., Murray, E., Zou, L.S., Goeva, A., Macosko, E.Z., Chen, F., Irizarry, R.A.: Robust decomposition of cell type mixtures in spatial transcriptomics. Nature biotechnology **40**(4), 517–526 (2022)

[8] Kleshchevnikov, V., Shmatko, A., Dann, E., Aivazidis, A., King, H.W., Li, T., Elmentaite, R., Lomakin, A., Kedlian, V., Gayoso, A., *et al.*: Cell2location maps fine-grained cell types in spatial transcriptomics. Nature biotechnology **40**(5), 661–671 (2022)

[9] Elosua-Bayes, M., Nieto, P., Mereu, E., Gut, I., Heyn, H.: Spotlight: seeded nmf regression to deconvolute spatial transcriptomics spots with single-cell transcriptomes. Nucleic acids research **49**(9), 50–50 (2021)

[10] Biancalani, T., Scalia, G., Buffoni, L., Avasthi, R., Lu, Z., Sanger, A., Tokcan, N., Vanderburg, C.R., Segerstolpe, Å., Zhang, M., *et al.*: Deep learning and alignment of spatially resolved single-cell transcriptomes with Tangram. Nature methods **18**(11), 1352–1362 (2021)

[11] Qiao, C., Huang, Y.: Reliable imputation of spatial transcriptome with uncertainty estimation and spatial regularization. bioRxiv, 2023–01 (2023)

[12] Bergenstråhle, L., He, B., Bergenstråhle, J., Abalo, X., Mirzazadeh, R., Thrane, K., Ji, A.L., Andersson, A., Larsson, L., Stakenborg, N., *et al.*: Super-resolved spatial transcriptomics by deep data fusion. Nature biotechnology **40**(4), 476–479 (2022)

[13] Hu, J., Coleman, K., Zhang, D., Lee, E.B., Kadara, H., Wang, L., Li, M.: Deciphering tumor ecosystems at super resolution from spatial transcriptomics with TESLA. Cell systems **14**(5), 404–417 (2023)

[14] Zhang, D., Schroeder, A., Yan, H., Yang, H., Hu, J., Lee, M.Y., Cho, K.S., Susztak, K., Xu, G.X., Feldman, M.D., et al.: Inferring super-resolution tissue architecture by integrating spatial transcriptomics with histology. Nature Biotechnology, 1–6 (2024)

[15] Wan, X., Xiao, J., Tam, S.S.T., Cai, M., Sugimura, R., Wang, Y., Wan, X., Lin, Z., Wu, A.R., Yang, C.: Integrating spatial and single-cell transcriptomics data using deep generative models with spatialscope. Nature Communications **14**(1), 7848 (2023)

[16] Pang, M., Su, K., Li, M.: Leveraging information in spatial transcriptomics to predict super-resolution gene expression from histology images in tumors. bioRxiv, 2021–11 (2021)

[17] He, B., Bergenstråhle, L., Stenbeck, L., Abid, A., Andersson, A., Borg, Å., Maaskola, J., Lundeberg, J., Zou, J.: Integrating spatial gene expression and breast tumour morphology via deep learning. Nature biomedical engineering **4**(8), 827–834 (2020)

[18] Graham, S., Vu, Q.D., Raza, S.E.A., Azam, A., Tsang, Y.W., Kwak, J.T., Rajpoot, N.: Hover-net: Simultaneous segmentation and classification of nuclei in multi-tissue histology images. Medical image analysis **58**, 101563 (2019)

[19] Fu, Y., Jung, A.W., Torne, R.V., Gonzalez, S., Vöhringer, H., Shmatko, A., Yates, L.R., Jimenez-Linan, M., Moore, L., Gerstung, M.: Pan-cancer computational histopathology reveals mutations, tumor composition and prognosis. Nature cancer **1**(8), 800–810 (2020)

[20] Zeng, Y., Wei, Z., Yu, W., Yin, R., Yuan, Y., Li, B., Tang, Z., Lu, Y., Yang, Y.: Spatial transcriptomics prediction from histology jointly through transformer and graph neural networks. Briefings in Bioinformatics **23**(5), 297 (2022)

[21] Jia, Y., Liu, J., Chen, L., Zhao, T., Wang, Y.: Thitogene: a deep learning method for predicting spatial transcriptomics from histological images. Briefings in Bioinformatics **25**(1), 464 (2024)

[22] Xie, R., Pang, K., Bader, G.D., Wang, B.: Spatially Resolved Gene Expression Prediction from H&E Histology Images via Bi-modal Contrastive Learning. arXiv preprint arXiv:2306.01859 (2023)

[23] Comiter, C., Vaishnav, E.D., Ciapmricotti, M., Li, B., Yang, Y., Rodig, S.J., Turner, M., Pfaff, K.L., Jané-Valbuena, J., Slyper, M., et al.: Inference of single cell profiles from histology stains with the single-cell omics from histology analysis framework (schaf). BioRxiv, 2023–03 (2023)

[24] Madissoon, E., Oliver, A.J., Kleshchevnikov, V., Wilbrey-Clark, A., Polanski, K., Richoz, N., Ribeiro Orsi, A., Mamanova, L., Bolt, L., Elmentaite, R., *et al.*: A spatially resolved atlas of the human lung characterizes a gland-associated immune niche. Nature Genetics **55**(1), 66–77 (2023)

[25] Andersson, A., Larsson, L., Stenbeck, L., Salmén, F., Ehinger, A., Wu, S.Z., Al-Eryani, G., Roden, D., Swarbrick, A., Borg, Å., *et al.*: Spatial deconvolution of her2-positive breast cancer delineates tumor-associated cell type interactions. Nature communications **12**(1), 6012 (2021)

[26] Li, Z., Wang, T., Liu, P., Huang, Y.: Spatialdm: Rapid identification of spatially co-expressed ligand-receptor reveals cell-cell communication patterns. bioRxiv, 2022–08 (2022)

[27] Buggert, M., Price, D.A., Mackay, L.K., Betts, M.R.: Human circulating and tissue-resident memory cd8+ t cells. Nature Immunology, 1–11 (2023)

[28] Davis, J.D., Wypych, T.P.: Cellular and functional heterogeneity of the airway epithelium. Mucosal immunology **14**(5), 978–990 (2021)

[29] Shaban, M., Bai, Y., Qiu, H., Mao, S., Yeung, J., Yeo, Y.Y., Shanmugam, V., Chen, H., Zhu, B., Nolan, G.P., et al.: Maps: Pathologist-level cell type annotation from tissue images through machine learning. bioRxiv (2023)

[30] Hu, T., Allam, M., Cai, S., Henderson, W., Yueh, B., Garipcan, A., Ievlev, A.V., Afkarian, M., Beyaz, S., Coskun, A.F.: Single-cell spatial metabolomics with cell-type specific protein profiling for tissue systems biology. Nature Communications **14**(1), 8260 (2023)

[31] Zahir, N., Sun, R., Gallahan, D., Gatenby, R.A., Curtis, C.: Characterizing the ecological and evolutionary dynamics of cancer. Nature genetics **52**(8), 759–767 (2020)

[32] Bartoschek, M., Oskolkov, N., Bocci, M., Lövrot, J., Larsson, C., Sommarin, M., Madsen, C.D., Lindgren, D., Pekar, G., Karlsson, G., *et al.*: Spatially and functionally distinct subclasses of breast cancer-associated fibroblasts revealed by single cell rna sequencing. Nature communications **9**(1), 5150 (2018)

[33] Hein, S.M., Haricharan, S., Johnston, A.N., Toneff, M.J., Reddy, J.P., Dong, J., Bu, W., Li, Y.: Luminal epithelial cells within the mammary gland can produce basal cells upon oncogenic stress. Oncogene **35**(11), 1461–1467 (2016)

[34] Seow, D.Y.B., Yeong, J.P.S., Lim, J.X., Chia, N., Lim, J.C.T., Ong, C.C.H., Tan, P.H., Iqbal, J.: Tertiary lymphoid structures and associated plasma cells play an important role in the biology of triple-negative breast cancers. Breast Cancer Research and Treatment **180**, 369–377 (2020)

[35] DeNardo, D.G., Andreu, P., Coussens, L.M.: Interactions between lymphocytes and myeloid cells regulate pro-versus anti-tumor immunity. Cancer and Metastasis Reviews **29**, 309–316 (2010)

[36] Ståhl, P.L., Salmén, F., Vickovic, S., Lundmark, A., Navarro, J.F., Magnusson, J., Giacomello, S., Asp, M., Westholm, J.O., Huss, M., *et al.*: Visualization and analysis of gene expression in tissue sections by spatial transcriptomics. Science **353**(6294), 78–82 (2016)

[37] Kumar, T., Nee, K., Wei, R., He, S., Nguyen, Q.H., Bai, S., Blake, K., Gong, Y., Pein, M., Sei, E., et al.: A spatially resolved single cell genomic atlas of the adult human breast. bioRxiv, 2023–04 (2023)

[38] Li, B., Eliceiri, K.W.: Dual-stream maximum self-attention multi-instance learning. arXiv preprint arXiv:2006.05538 (2020)

[39] Yang, Y., Hossain, M.Z., Stone, E.A., Rahman, S.: Exemplar guided deep neural network for spatial transcriptomics analysis of gene expression prediction. In: Proceedings of the IEEE/CVF Winter Conference on Applications of Computer Vision, pp. 5039–5048 (2023)

[40] Yang, Y., Hossain, M.Z., Stone, E., Rahman, S.: Spatial transcriptomics analysis of gene expression prediction using exemplar guided graph neural network. Pattern Recognition **145**, 109966 (2024)

[41] He, K., Zhang, X., Ren, S., Sun, J.: Deep residual learning for image recognition. In: Proceedings of

the IEEE Conference on Computer Vision and Pattern Recognition, pp. 770–778 (2016)

[42] Russakovsky, O., Deng, J., Su, H., Krause, J., Satheesh, S., Ma, S., Huang, Z., Karpathy, A., Khosla, A., Bernstein, M., *et al.*: Imagenet large scale visual recognition challenge. International journal of computer vision **115**, 211–252 (2015)

[43] Wu, Z., Jain, P., Wright, M., Mirhoseini, A., Gonzalez, J.E., Stoica, I.: Representing long-range context for graph neural networks with global attention. Advances in Neural Information Processing Systems **34**, 13266–13279 (2021)

[44] Rong, Y., Bian, Y., Xu, T., Xie, W., Wei, Y., Huang, W., Huang, J.: Self-supervised graph transformer on large-scale molecular data. Advances in Neural Information Processing Systems **33**, 12559–12571 (2020)

[45] Brody, S., Alon, U., Yahav, E.: How attentive are graph attention networks? arXiv preprint arXiv:2105.14491 (2021)

[46] Vaswani, A., Shazeer, N., Parmar, N., Uszkoreit, J., Jones, L., Gomez, A.N., Kaiser, Ł., Polosukhin, I.: Attention is all you need. Advances in neural information processing systems **30** (2017)

[47] Ba, J.L., Kiros, J.R., Hinton, G.E.: Layer normalization. arXiv preprint arXiv:1607.06450 (2016)

[48] Wartenberg, D.: Multivariate spatial correlation: A method for exploratory geographical analysis. Geographical Analysis **17**, 263–283 (2010) https://doi.org/10.1111/j.1538-4632.1985.tb00849.x

9 Supplementary

Supplementary Fig 1: UMAP representation of 80 cell types identified by Louvain clustering on the reference single cell reference dataset of human lung dataset.

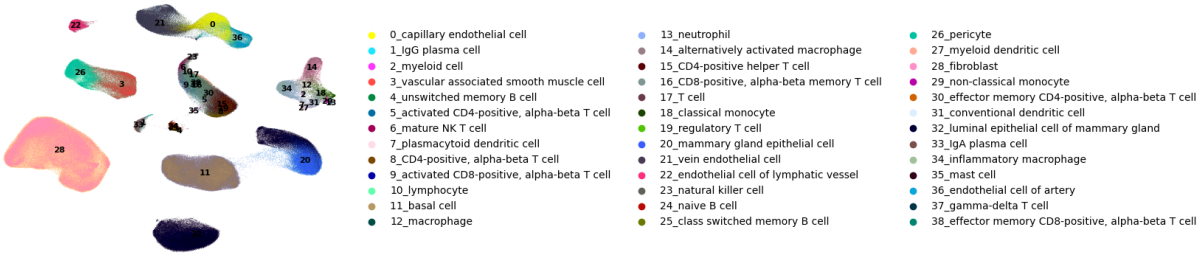

Supplementary Fig 2: UMAP representation of 39 cell types identified by Louvain clustering on the reference single cell reference dataset of human breast cancer dataset.

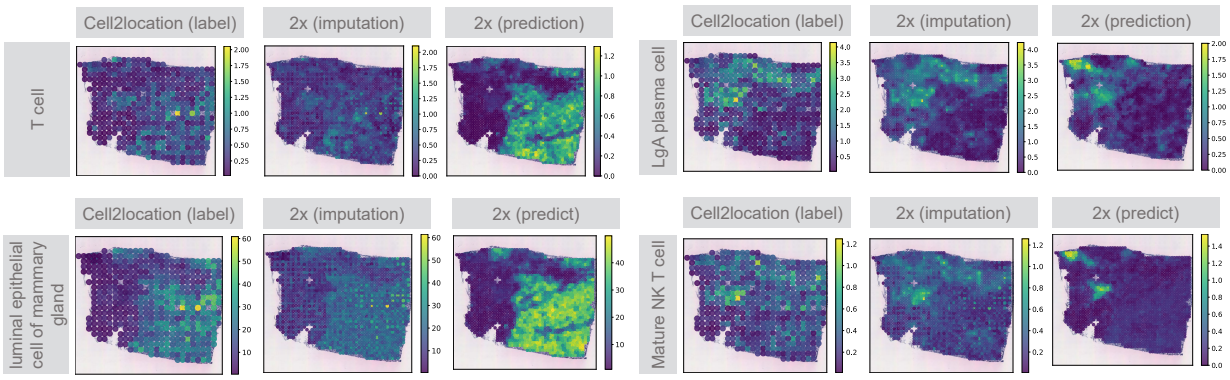

Supplementary Fig 3: **Hist2Cell provides super-resolved spatial cell abundances with more accurate alignment to tumor/normal annotation than STNet.** Visualizations comparing low-resolution ground truth cell abundance with both imputed and directly predicted high-resolution results by Hist2Cell. Both approaches provide a more detailed mapping in concordance with the tumor/normal annotation shown in Fig. 4.c.

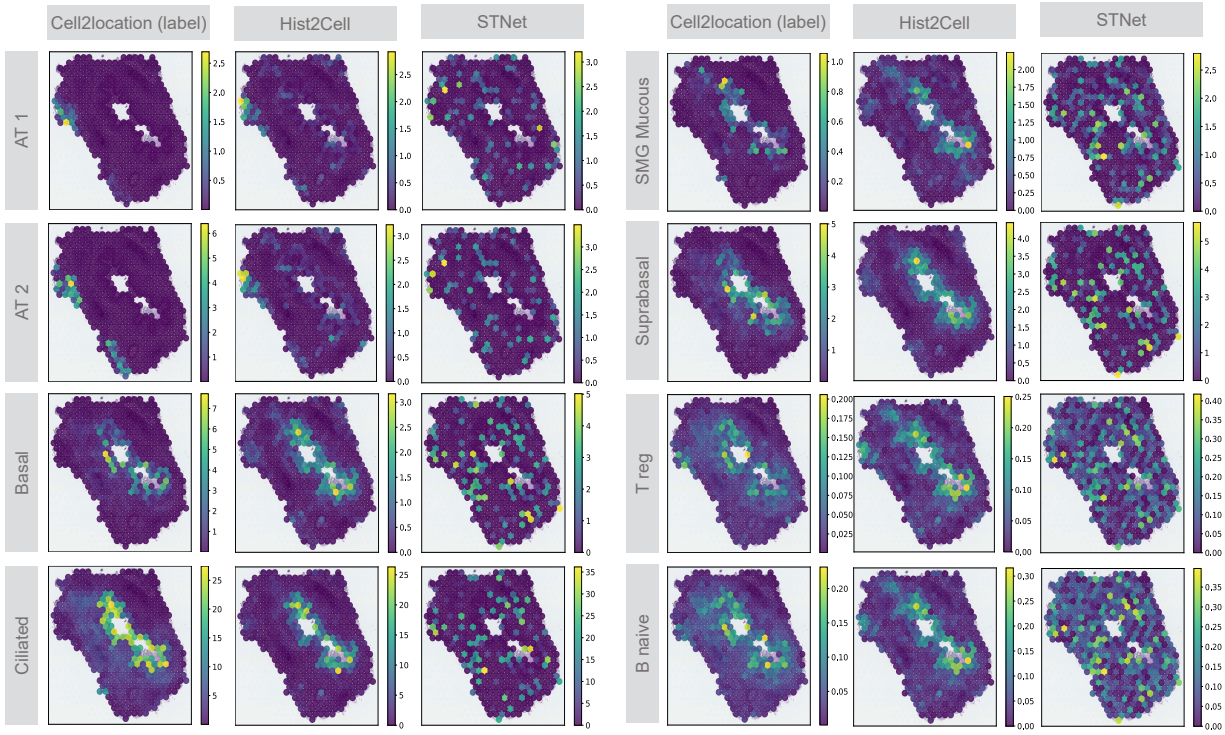

Supplementary Fig 4: Hist2Cell provide more accurate alignment to manual annotation than STNet. The visualizations comparing the spatial cell abundances as determined by ground truth, Hist2Cell, and STNet predictions for select key cell types. Hist2Cell show less false positives than STNet when comparing to both ground truth and manual annotation in Fig.3.b.

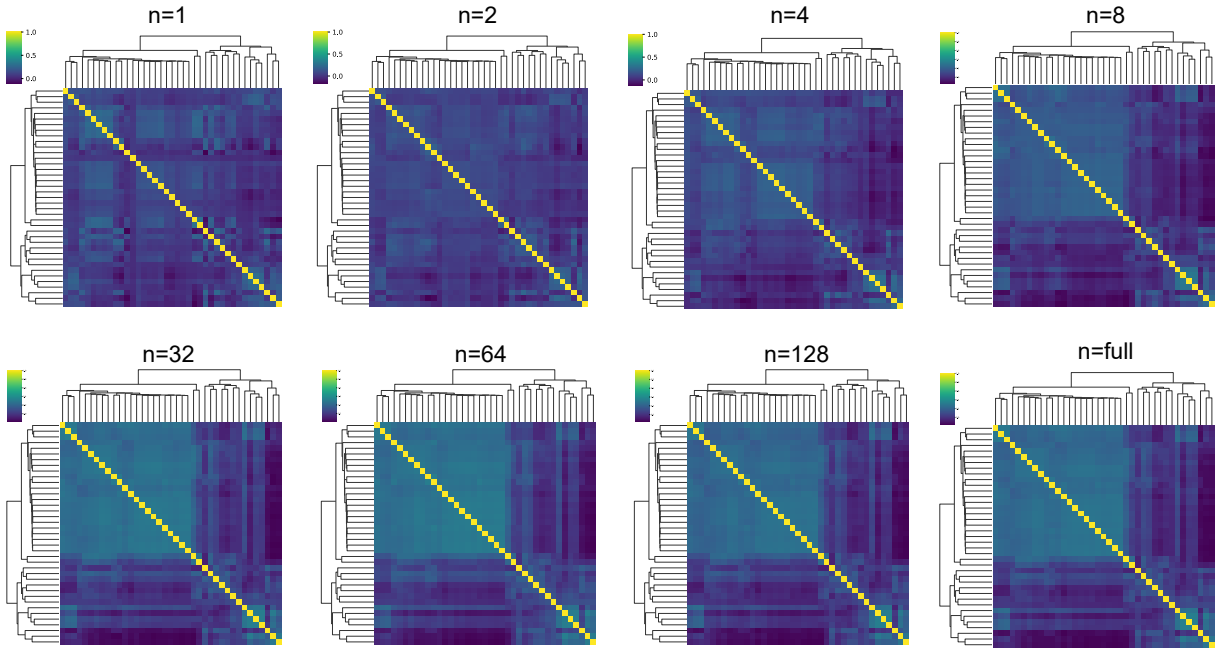

Supplementary Fig 5: Hist2Cell provides more stabilized consensus analysis with larger sample sizes. Consensus clustermaps generated by Hist2Cell using varying numbers of samples from the TCGA breast cancer cohort. n denotes the number of randomly sampled slides, with $n =$ full indicating the use of the entire cohort. The consensus clustermaps become more stable as the number of sampled slides increases.

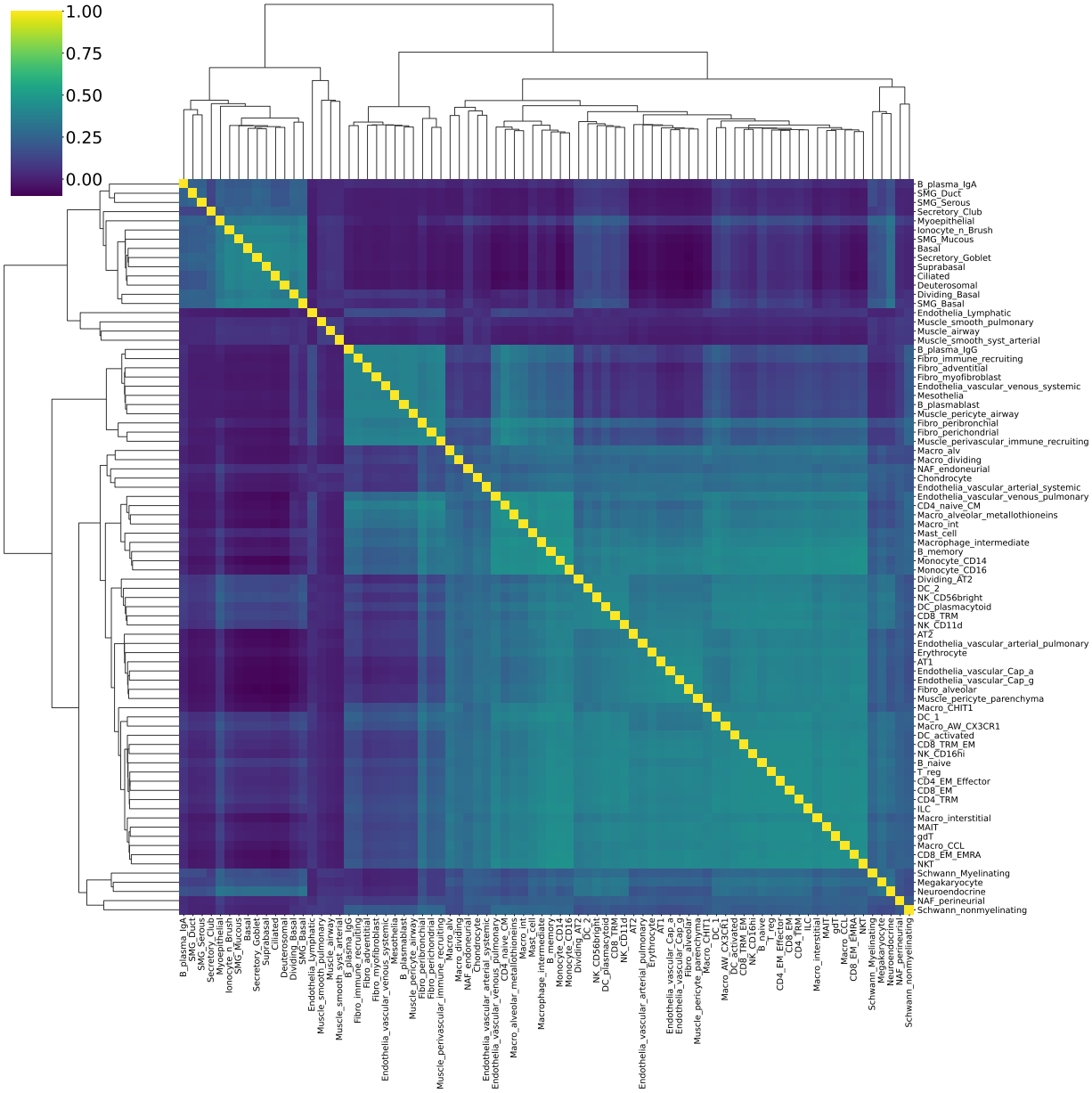

Supplementary Fig 6: Detailed Human lung Moran's R Clustermaps calculated from ground truth cell type abundances (cell2location algorithm) in Fig.2e.

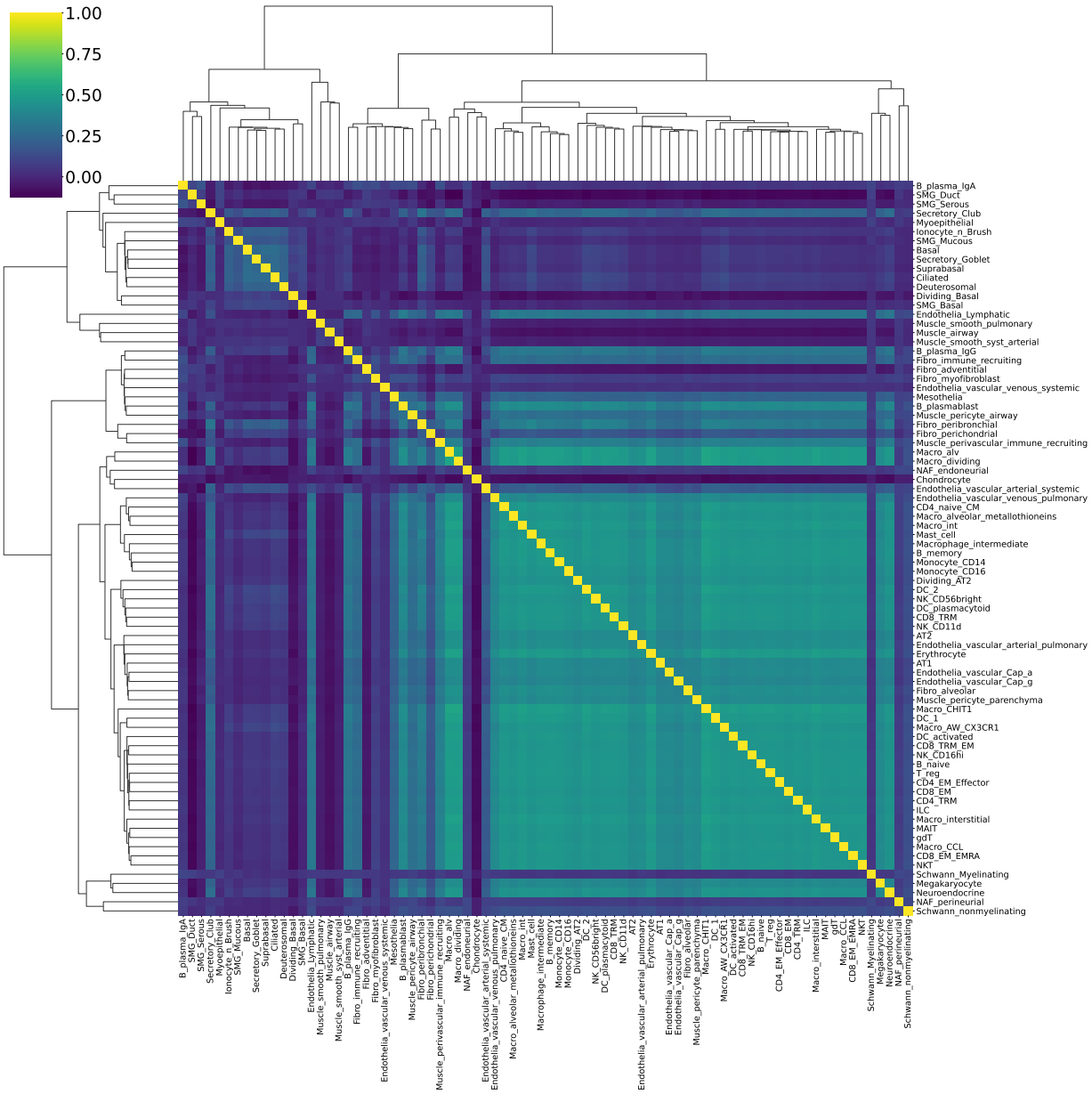

Supplementary Fig 7: Detailed Human lung Moran's R Clustermaps calculated from Hist2Cell predictions in Fig.2e.

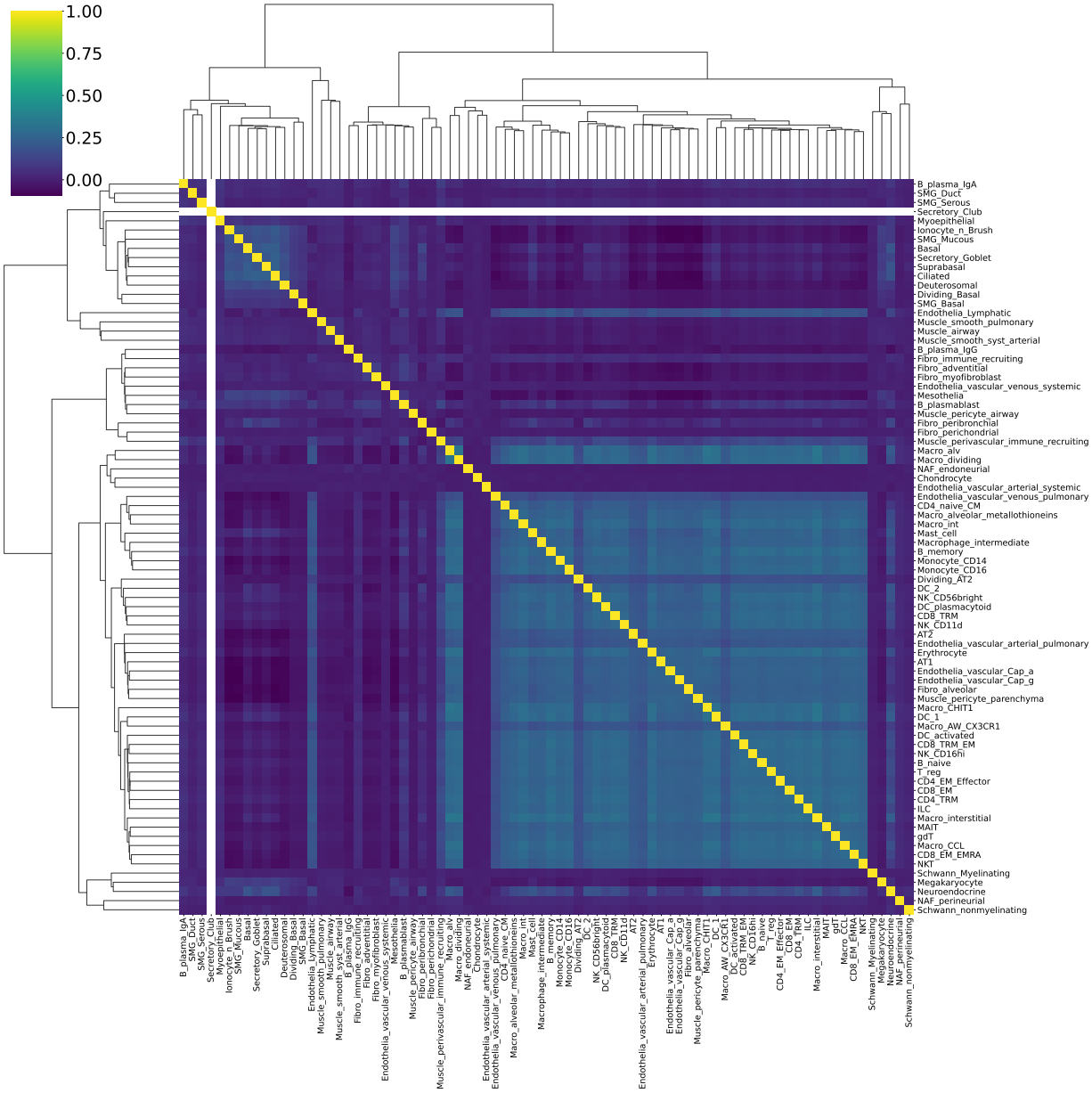

Supplementary Fig 8: Detailed Human lung Moran's R Clustermaps calculated from STNet predictions in Fig.2e.

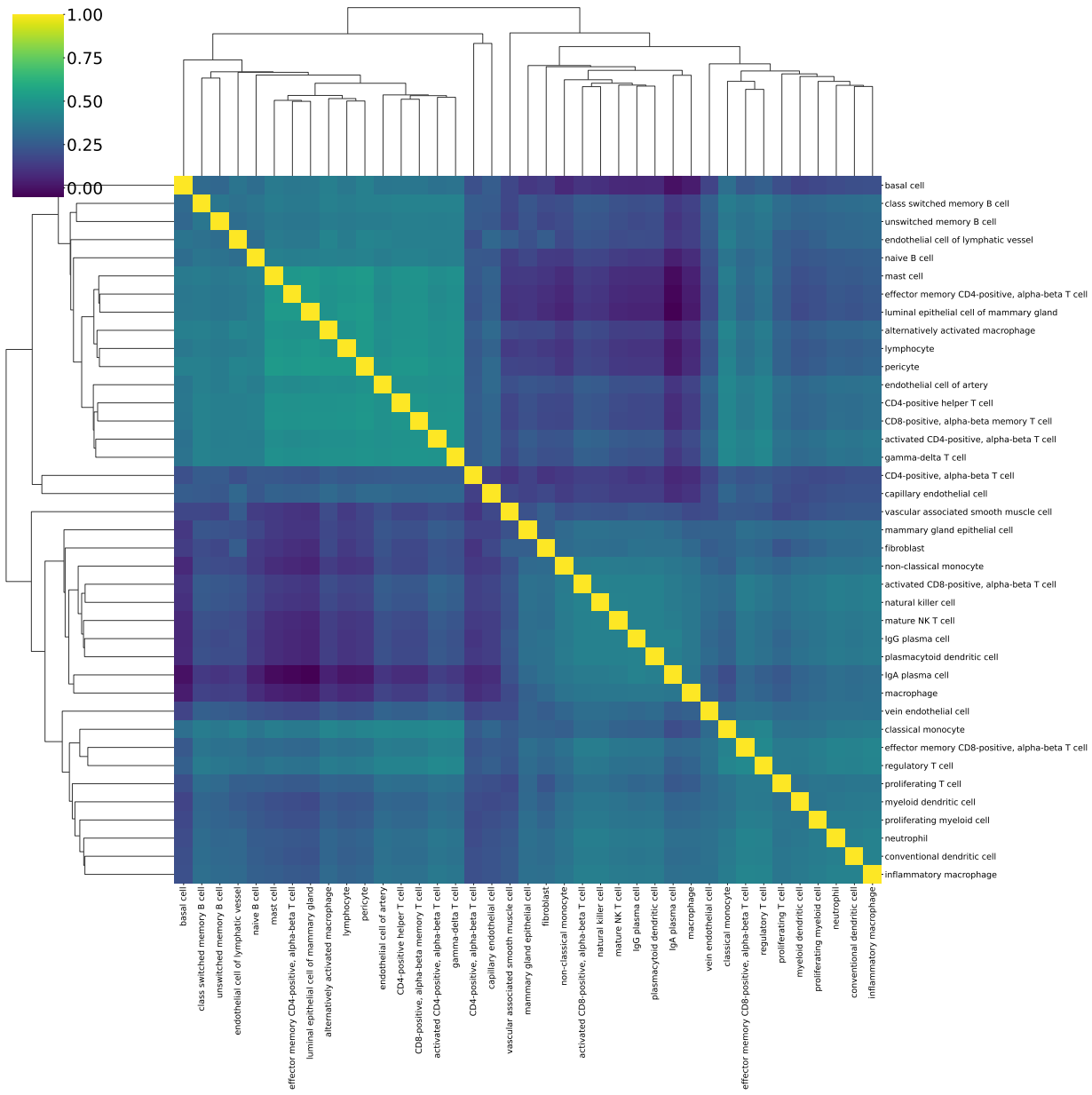

Supplementary Fig 9: Detailed Human breast cancer Moran's R Clustermaps calculated from ground truth cell type abundances (cell2location algorithm) in Fig.4.e.

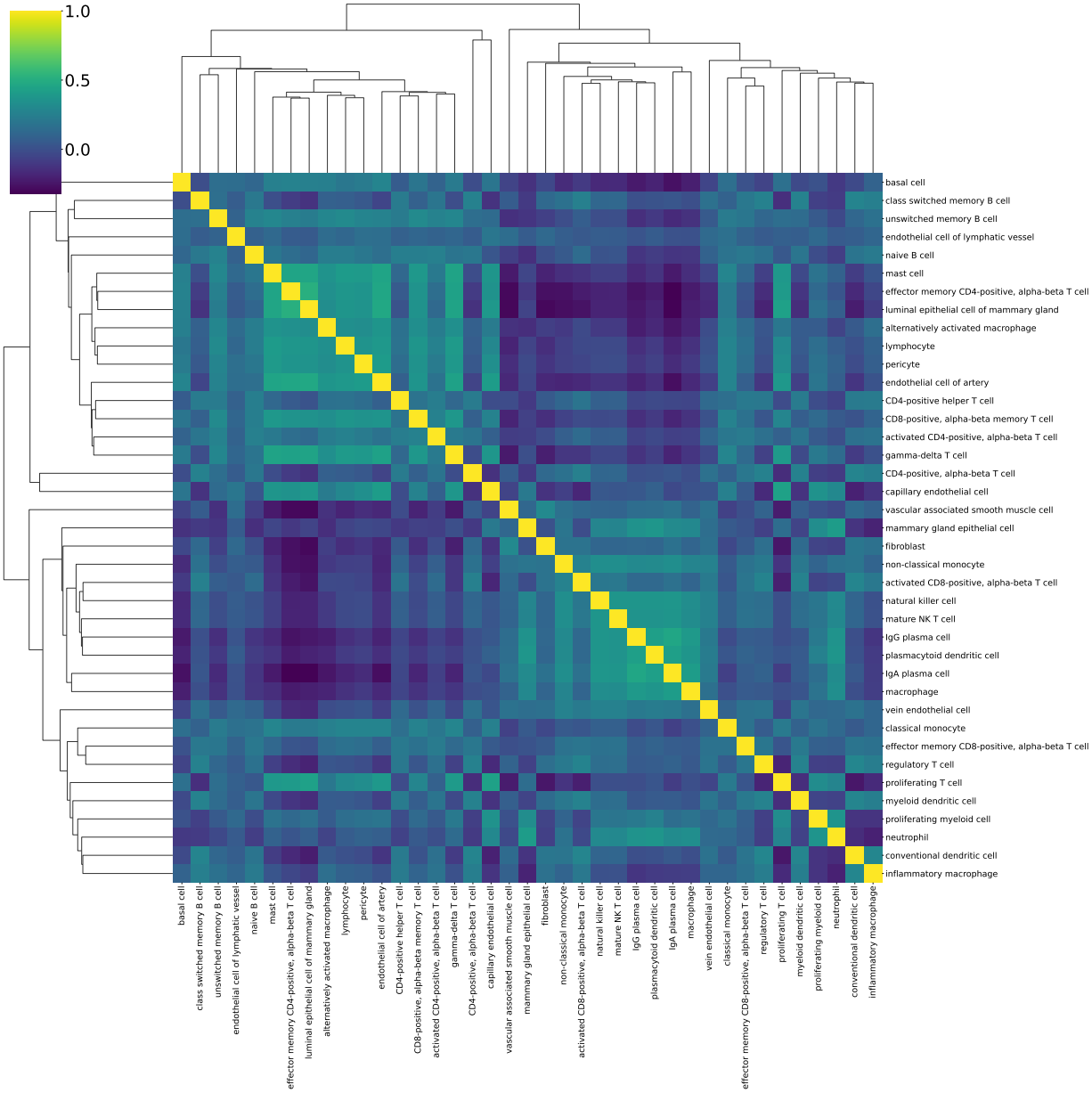

Supplementary Fig 10: Detailed Human breast cancer Moran's R Clustermaps calculated from Hist2Cell predictions in Fig.4.e.

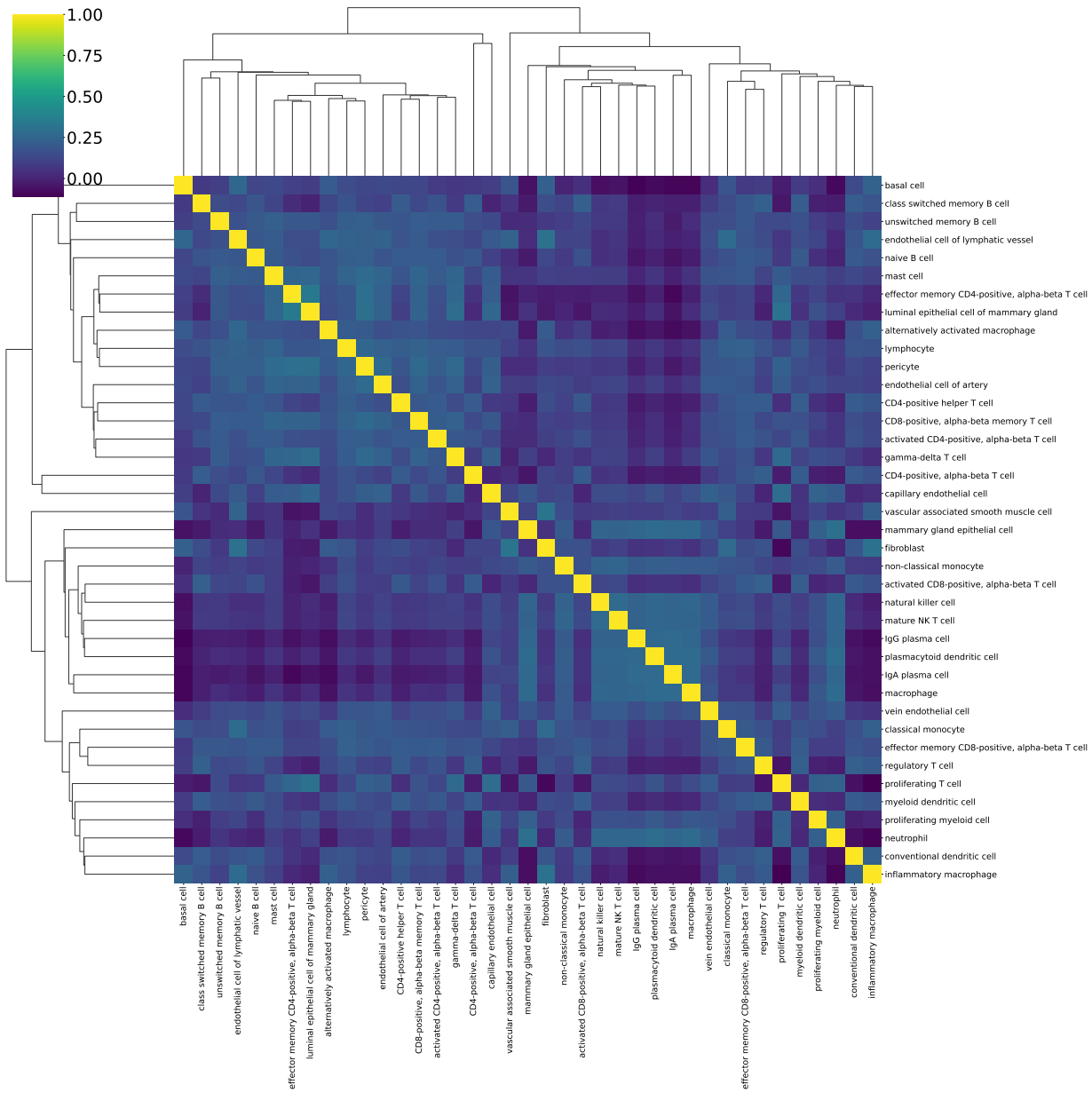

Supplementary Fig 11: Detailed Human breast cancer Moran's R Clustermaps calculated from STNet predictions in Fig.4.e.